PI3K signaling and adherens junctions in invasive lobular breast cancer

Klarenbeek, S.

5

PTEN loss in E-cadherin-deficient mouse mammary epithelial cells rescues apoptosis and results in development of classical invasive lobular carcinoma

Mirjam C. Boelens[1,#], Micha Nethe[1,#], Sjoerd Klarenbeek[1,#], Julian R. de Ruiter[1], Eva Schut[1], Nicola Bonzanni[2], Amber L. Zeeman[3], Ellen Wientjens[1], Eline van der Burg[1], Lodewyk Wessels[2], Renée van Amerongen[3], Jos Jonkers[4]

[#] contributed equally

[1] Division of Molecular Pathology, the Netherlands Cancer Institute, Amsterdam, the Netherlands

[2] Division of Molecular Carcinogenesis, the Netherlands Cancer Institute, Amsterdam, the Netherlands

[3] Section of Molecular Cytology and Van Leeuwenhoek Centre for Advanced Microscopy, University of Amsterdam, Amsterdam, the Netherlands

[4] Cancer Genomics Netherlands, Utrecht, the Netherlands

Cell Reports 16, 2087-2101 (2016)

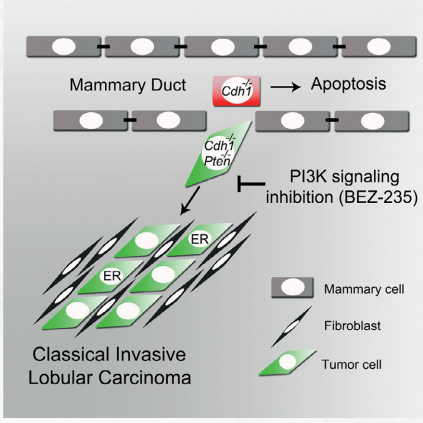

ABSTRACT

Invasive lobular carcinoma (ILC) is an aggressive breast cancer subtype with poor response to chemotherapy. Besides loss of E-cadherin, a hallmark of ILC, genetic inactivation of PTEN is frequently observed in patients. Through concomitant Cre-mediated inactivation of E-cadherin and PTEN in mammary epithelium, we generated a mouse model of classical ILC (CLC), the main histological ILC subtype. While loss of E-cadherin induced cell dissemination and apoptosis, additional PTEN inactivation promoted cell survival and rapid formation of invasive mammary tumors that recapitulate the histological and molecular features, estrogen receptor (ER) status, growth kinetics, metastatic behavior, and tumor microenvironment of human CLC. Combined inactivation of E-cadherin and PTEN is sufficient to cause CLC development. These CLCs showed significant tumor regression upon BEZ235-mediated inhibition of PI3K signaling. In summary, this mouse model provides important insights into CLC development and suggests inhibition of phosphatidylinositol 3-kinase (PI3K) signaling as a potential therapeutic strategy for targeting CLC.

INTRODUCTION

Invasive lobular carcinoma (ILC) is the second most common subtype of breast cancer, comprising 8%–14% of all breast cancer cases (Li et al., 2003, Pestalozzi et al., 2008). ILC is histologically characterized by single-cell files of tumor cells in a fibrous stroma. Due to its invasive growth behavior, this tumor type does not immediately form a defined tumor mass and, therefore, is difficult to detect by physical examination or mammography (Houssami et al., 2003). Despite being classified as a histologic low-grade tumor type with a low-to-intermediate mitotic index, the infiltrating nature of ILC complicates surgical removal. Moreover, ILCs typically respond poorly to classical regimes of chemotherapy. To improve treatment options, more insight into ILC development is required.

On the molecular level, ILC is characterized by loss of the cell-adhesion protein E-cadherin (Moll et al., 1993), an event that has been shown to drive tumor invasion. Nevertheless, somatic inactivation of E-cadherin in mouse mammary epithelium does not induce spontaneous mammary tumor development (Boussadia et al., 2002, Derksen et al., 2006), indicating that additional (epi)genetic lesions are required for ILC formation. Activation of the phosphatidylinositol 3-kinase (PI3K) pathway, as displayed by either activating *PIK3CA* mutations or homozygous deletions or inactivating mutations in *PTEN*, is frequently observed in ILC (Buttitta et al., 2006, Ciriello et al., 2015, Michaut et al., 2016, Michelucci et al., 2009). PI3K signaling controls multiple cellular processes, such as cell proliferation, survival, and migration, by the conversion of phosphatidylinositol 4,5-bisphosphate (PIP_2) to phosphatidylinositol (3,4,5)-trisphosphate (PIP_3), driving activation of downstream targets such as AKT. To test whether constitutive activation of PI3K signaling can, indeed, drive the formation of ILC, we generated mice with mammary-specific Cre-conditional inactivation of E-cadherin and PTEN. We found that combined loss of both E-cadherin and PTEN in mouse mammary epithelial cells induces mouse mammary tumors that closely resemble classical invasive lobular carcinoma (CLC), the main subtype of human ILC.

RESULTS

Inactivation of E-Cadherin and PTEN In Vitro Alters Growth and Invasion of Mammary Epithelium

To study the direct consequence of inactivation of E-cadherin (encoded by the *Cdh1* gene) and PTEN in primary mammary epithelial cells, we generated mammary organoids from *Cdh1*$^{F/F}$;*Pten*$^{F/F}$ mice (Derksen et al., 2006, Ma et al., 2005). In vitro transduction of

organoids using a Cre-recombinase-encoding adenovirus (AdCre) allowed us to test the direct effects of E-cadherin and PTEN loss in mammary epithelium. To confirm efficient AdCre-mediated recombination in vitro, we used organoids from *mTmG* reporter mice that express tandem dimer Tomato (tdT) prior to recombination and GFP after Cre-mediated excision of tdT (Muzumdar et al., 2007). AdCre transduction of *mTmG* organoids induced loss of tdT and expression of GFP in nearly all cells (Figure S1A). Importantly, the phenotype of AdCre-transduced *mTmG* organoids appeared unaltered as compared to non-transduced organoids from the same mouse, indicating that organoid growth rate and phenotype are not affected by AdCre transduction (Figure S1A). This strategy was, therefore, applied to inactivate E-cadherin and/or PTEN in $Cdh1^{F/F}$, $Pten^{F/F}$, and $Cdh1^{F/F};Pten^{F/F}$ organoids, respectively. All non-transduced organoids displayed similar-sized cyst-like structures after 7 days of culture (Figure S1B). The inactivation of E-cadherin altered mammary organoid phenotype by inducing discohesive cellular structures surrounding the organoid cores, while the inactivation of PTEN resulted in enlarged smooth-edged organoids (Figure S1B). Concurrent inactivation of E-cadherin and PTEN revealed a combined phenotype of $Cdh1^{\Delta/\Delta}$ and $Pten^{\Delta/\Delta}$ organoids, as $Cdh1^{\Delta/\Delta};Pten^{\Delta/\Delta}$ organoids were both enlarged and showed discohesive cellular structures (Figure S1B). Efficient recombination was confirmed by western blotting and PCR, showing strong reduction of E-cadherin and/or PTEN protein expression and deletion of the $Cdh1^{F}$ and $Pten^{F}$ alleles, respectively (Figures 1A and S1C). In addition, AdCre-transduced $Pten^{F/F}$ and $Cdh1^{F/F};Pten^{F/F}$ organoids showed a strong induction of AKT phosphorylation, indicating activation of PI3K signaling due to PTEN loss (Figure 1A).

To study the long-term consequences of E-cadherin and/or PTEN loss in mammary epithelial cells, we monitored organoid development over a period of 21 days. Non-transduced organoids from each genotype decreased similarly in size and were hardly detectable after 21 days of culture (Figure 1B). The size of $Cdh1^{\Delta/\Delta}$ organoids remained stable, while the size of $Pten^{\Delta/\Delta}$ and $Cdh1^{\Delta/\Delta};Pten^{\Delta/\Delta}$ organoids continued to increase (Figures 1B and 1C). Again, the margins of both $Cdh1^{\Delta/\Delta}$ and $Cdh1^{\Delta/\Delta};Pten^{\Delta/\Delta}$ organoids showed discohesive cellular structures (Figure 1B).

To examine why growth kinetics differed between $Cdh1^{\Delta/\Delta}$ and $Cdh1^{\Delta/\Delta};Pten^{\Delta/\Delta}$ organoids, we analyzed cell proliferation and apoptosis by immunofluorescence (IF) with antibodies against Ki-67 and cleaved caspase-3 (CC3), respectively. $Cdh1^{\Delta/\Delta}$ organoids showed a balanced number of cells in proliferation or apoptosis, which might explain their sustained size over time (Figures 1D and 1E). Consistent with a survival role for the PI3K signaling pathway, both $Pten^{\Delta/\Delta}$ and $Cdh1^{\Delta/\Delta};Pten^{\Delta/\Delta}$ organoids showed almost no apoptotic cells (Figure 1E), resulting in an increase in organoid size over time (Figures 1B and 1C).

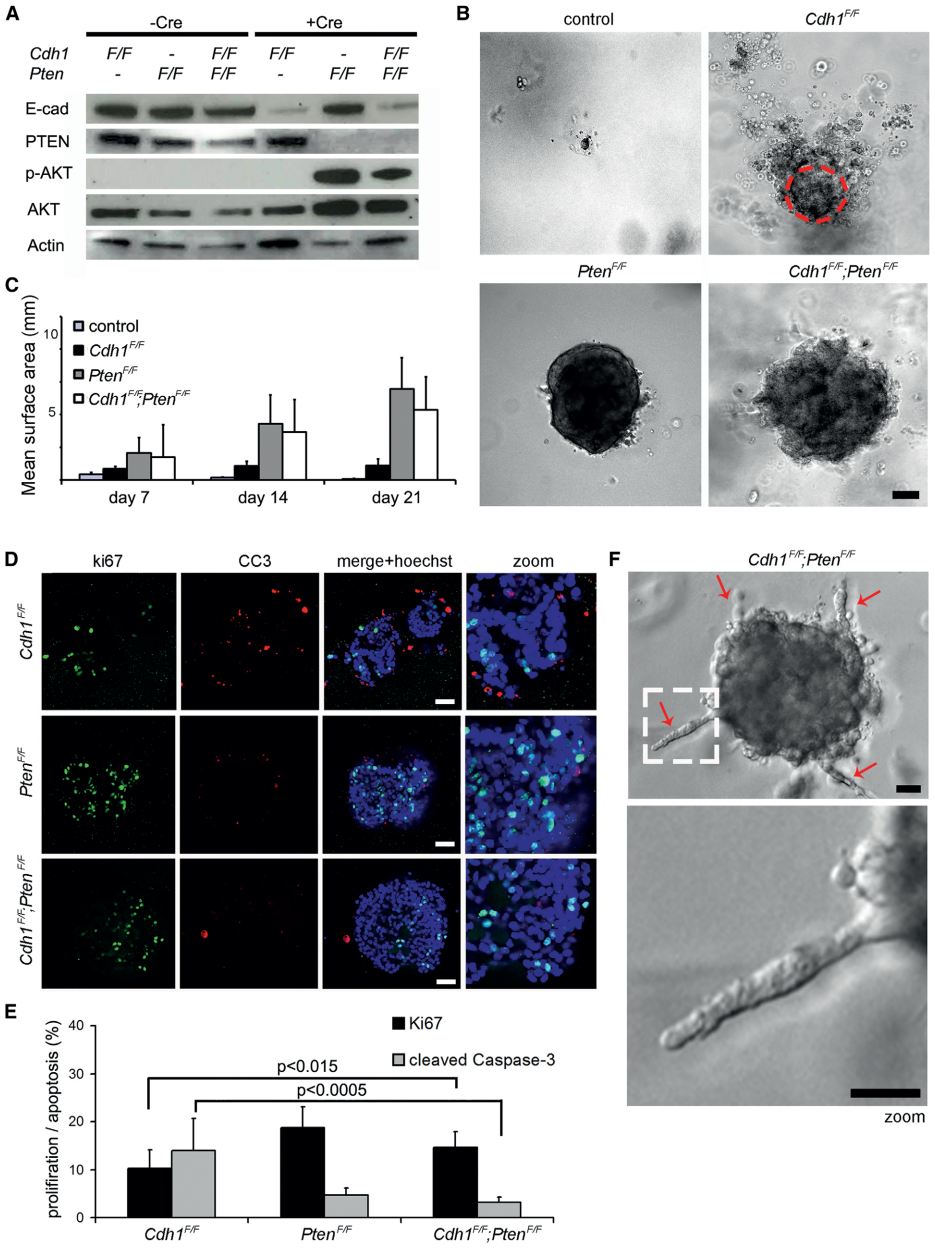

Figure 1. Inactivation of E-Cadherin and PTEN Alters Mammary Epithelial Morphology and Growth In Vitro

(A) Western blot analyses of E-cadherin, PTEN, and p-AKT(Ser473)/AKT protein expression of untransduced and AdCre-transduced *Cdh1*$^{F/F}$, *Pten*$^{F/F}$, and *Cdh1*$^{F/F}$;*Pten*$^{F/F}$ mammary organoids.

(B) Representative bright-field images of untransduced and AdCre-transduced *Cdh1*$^{F/F}$, *Pten*$^{F/F}$, and *Cdh1*$^{F/F}$;*Pten*$^{F/F}$ mammary organoids at day 21 of organoid culture. The dashed circle depicts the surface size of AdCre-transduced *Cdh1*$^{F/F}$ organoids. Scale bar, 50 µm.

(C) Average measurements of surface size (n = 10 per genotype) of untransduced and AdCre-transduced *Cdh1*$^{F/F}$, *Pten*$^{F/F}$, and *Cdh1*$^{F/F}$;*Pten*$^{F/F}$ organoids at days 7, 14, and 21 of organoid culture.
(D) Expression of Ki67 and CC3 measured by whole-mount immunostaining of AdCre-transduced *Cdh1*$^{F/F}$, *Pten*$^{F/F}$, and *Cdh1*$^{F/F}$;*Pten*$^{F/F}$ organoids. Scale bars, 50 μm.
(E) Quantification of the fraction of Ki67- and CC3-positive cells over the total cell number (determined by Hoechst) in AdCre-transduced *Cdh1*$^{F/F}$, *Pten*$^{F/F}$, and *Cdh1*$^{F/F}$;*Pten*$^{F/F}$ (n = 10 per genotype).
(F) Representative bright-field images of a *Cdh1*$^{F/F}$;*Pten*$^{F/F}$ organoid displaying invasive protrusions of single rows of cells (arrows) 1 day after medium change. Scale bars, 25 μm.

In contrast to *Pten*$^{\Delta/\Delta}$ organoids, *Cdh1*$^{\Delta/\Delta}$;*Pten*$^{\Delta/\Delta}$ organoids displayed an invasive response upon renewal of the cell culture medium (Figures 1F and S1D). These invasive cellular strands displayed single files of cells, indicating an increased invasive potential of *Cdh1*$^{\Delta/\Delta}$;*Pten*$^{\Delta/\Delta}$ mammary epithelium upon stimulation by growth factors and/or chemoattractants in the culture medium.

Together, these observations suggest that PI3K pathway activation through the disruption of PTEN can rescue apoptosis induced by E-cadherin loss in mammary epithelial organoids, resulting in invasive and proliferative behavior in vitro.

Inactivation of E-Cadherin and PTEN in Mammary Epithelium In Vivo Induces Rapid Formation of Hyperplastic and Infiltrative Lesions

To study the consequences of E-cadherin and PTEN loss in vivo, we generated *Wcre;Cdh1*$^{F/F}$;*Pten*$^{F/F}$ female mice, in which mammary-epithelium-specific inactivation of E-cadherin and PTEN is induced by whey acidic protein (*WAP*) gene promoter-driven Cre recombinase (*Wcre*) (Derksen et al., 2006). We also generated *Wcre;Cdh1*$^{F/F}$ and *Wcre;Pten*$^{F/F}$ female mice to study the effects of E-cadherin or PTEN loss alone. Since *Wcre* activity is first detectable in the fourth week of mammary gland development (data not shown), we analyzed the consequences of somatic inactivation of E-cadherin and/or PTEN during mammary gland development. Histological analysis and immunohistochemistry (IHC) for cytokeratin 8 (CK8; marking luminal mammary epithelial cells) indicated inactivation of E-cadherin to cause hyperplastic and dysplastic ducts, as well as a marked accumulation of dissociated mammary epithelial cells in the lumen of mammary epithelium from 6-week-old *Wcre;Cdh1*$^{F/F}$ mice (Figure 2A). Inactivation of PTEN alone did not reveal distinct alterations in mammary epithelial composition in *Wcre;Pten*$^{F/F}$ (Figure 2A). In contrast, mammary epithelium from 6-week-old *Wcre;Cdh1*$^{F/F}$;*Pten*$^{F/F}$ mice displayed multifocal neoplastic lesions infiltrating the surrounding stroma (Figure 2A). Analysis of over 20 nulliparous *Wcre;Cdh1*$^{F/F}$;*Pten*$^{F/F}$ mice confirmed a robust synergy between loss of E-cadherin and PTEN in driving formation of these mammary epithelial lesions, as all mice displayed neoplastic lesions

at 6 weeks of age. The infiltration pattern of these neoplastic lesions showed strong resemblance with the characteristic trabecular and discohesive growth pattern of tumor cells in human CLC. We confirmed *Wcre*-mediated inactivation of E-cadherin and/or PTEN in luminal epithelial cells by IF (Figures 2B and S2A). Analysis of *Wcre;Cdh1*$^{F/F}$ glands showed that E-cadherin-deficient cells in the lumen are CK8 positive, indicating that these cells indeed dissociated from the luminal epithelium (Figure S2A). This phenomenon is likely caused by reduced junctional integrity following E-cadherin loss (Shamir et al., 2014). Even though *Wcre;Pten*$^{F/F}$ glands did not display neoplastic lesions within 6 weeks, we clearly observed stochastic loss of PTEN in luminal epithelial cells (Figure S2A). The neoplastic lesions observed in *Wcre;Cdh1*$^{F/F}$*;Pten*$^{F/F}$ mammary glands displayed discohesive CK8-marked luminal epithelial cells that, indeed, lost E-cadherin and PTEN, whereas surrounding stromal cells retained PTEN expression (Figure 2B). Moreover, E-cadherin-deficient cells still expressed CK8, indicating that these cells did not undergo epithelial-to-mesenchymal transition (EMT), as also previously observed (Derksen et al., 2006).

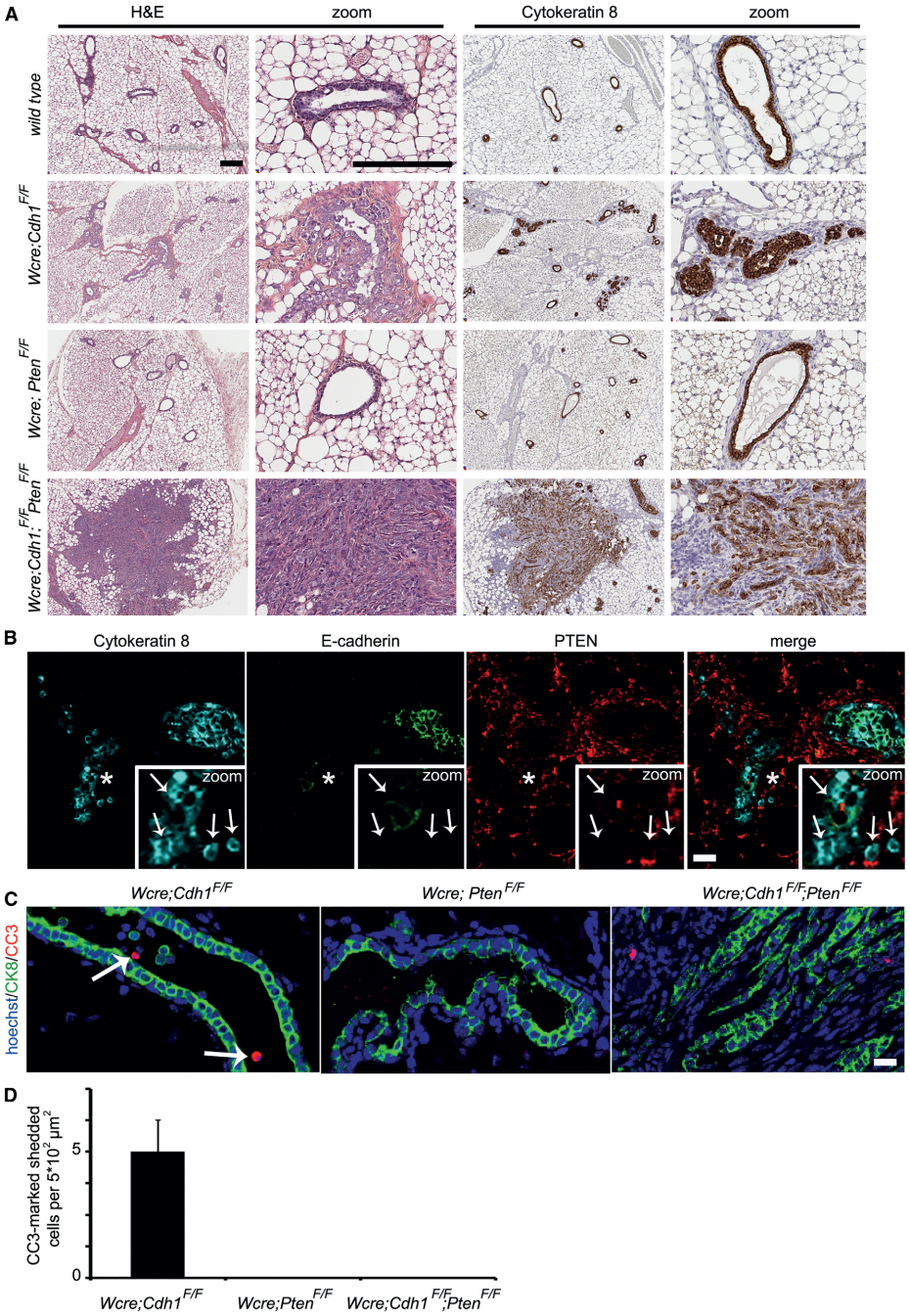

Figure 2. Inactivation of E-Cadherin and PTEN in Mammary Epithelium In Vivo Induces Rapid Formation of Neoplastic Lesions

(A) H&E staining and IHC of CK8 in mammary glands from 6-week-old wild-type, *Wcre;Cdh1$^{F/F}$*, *Wcre;Pten$^{F/F}$*,

and *Wcre;Cdh1$^{F/F}$;Pten$^{F/F}$* mice. Scale bars, 150 μm.
(B) IF analysis of CK8, E-cadherin, and PTEN in mammary glands from 6-week-old *Wcre;Cdh1$^{F/F}$;Pten$^{F/F}$* mice. Scale bar, 20 μm. Zooms of the asterisk-marked area reveal CK8-positive neoplastic cells that are negative for of E-cadherin and PTEN (indicated by arrows), flanked by PTEN-positive stromal cells.
(C) IF analysis of CK8 (green) and CC3 (red) in mammary glands from 6-week-old *Wcre;Cdh1$^{F/F}$;Pten$^{F/F}$* mice. Arrows mark CC3-positive apoptotic cells in the mammary duct. Scale bar, 20 μm.
(D) Average numbers of CC3-positive shedded cells per 500-μm^2 area in mammary gland sections from *Wcre;Cdh1$^{F/F}$, Wcre;Pten$^{F/F}$ and Wcre;Cdh1$^{F/F}$;Pten$^{F/F}$* mice.

Since inactivation of PTEN rescued apoptosis and promoted survival of E-cadherin-deficient mammary epithelial cells in *Cdh1$^{Δ/Δ}$;Pten$^{Δ/Δ}$* organoids, we analyzed apoptosis by CC3 IF staining in mammary gland sections from 6-week-old *Wcre;Cdh1$^{F/F}$*, *Wcre;Pten$^{F/F}$*, and *Wcre;Cdh1$^{F/F}$;Pten$^{F/F}$* mice. While no apoptosis was observed in *Wcre;Pten$^{F/F}$* and *Wcre;Cdh1$^{F/F}$;Pten$^{F/F}$* mammary glands, CK8-positive cells in the lumen of mammary ducts in *Wcre;Cdh1$^{F/F}$* mice displayed CC3-marked apoptosis (Figures 2C and 2D). Compared to *Cdh1$^{Δ/Δ}$* organoids, *Wcre;Cdh1$^{F/F}$* mammary glands showed only limited numbers of CC3-marked cells, most likely due to rapid clearance of apoptotic cells in the lumen of mammary ducts. These data underscore the notion that the loss of PTEN promotes survival of E-cadherin-deficient mammary epithelial cells through inhibition of apoptosis.

To further investigate the effects of concomitant inactivation of E-cadherin and PTEN on mammary gland development and functionality, we analyzed mammary gland outgrowth during puberty and mammary gland maturation during pregnancy in nine *Wcre;Cdh1$^{F/F}$;Pten$^{F/F}$* mice. Whole-mount analysis of mammary glands from 8-week-old *Wcre;Cdh1$^{F/F}$;Pten$^{F/F}$* mice showed, beside neoplastic lesions and hyperplastic ducts, a delay in mammary gland development, as compared to age-matched wild-type mammary glands (Figure S2B). Impaired mammary gland maturation was also observed during pregnancy, as pups from five 12-week-old *Wcre;Cdh1$^{F/F}$;Pten$^{F/F}$* mice grew poorly and died 6 days after birth, while littermates fostered onto wild-type dams showed normal weight and survival (Figure S2C). This phenomenon is likely caused by the reduced numbers of milk-producing glands in *Wcre;Cdh1$^{F/F}$;Pten$^{F/F}$* mice, as compared to wild-type foster dams (Figure S2D). Thus, both the development and maturation of *Cdh1$^{Δ/Δ}$;Pten$^{Δ/Δ}$* mammary epithelium is strongly impaired, which is likely caused by the loss of mammary epithelial integrity and formation of multi-focal neoplasia.

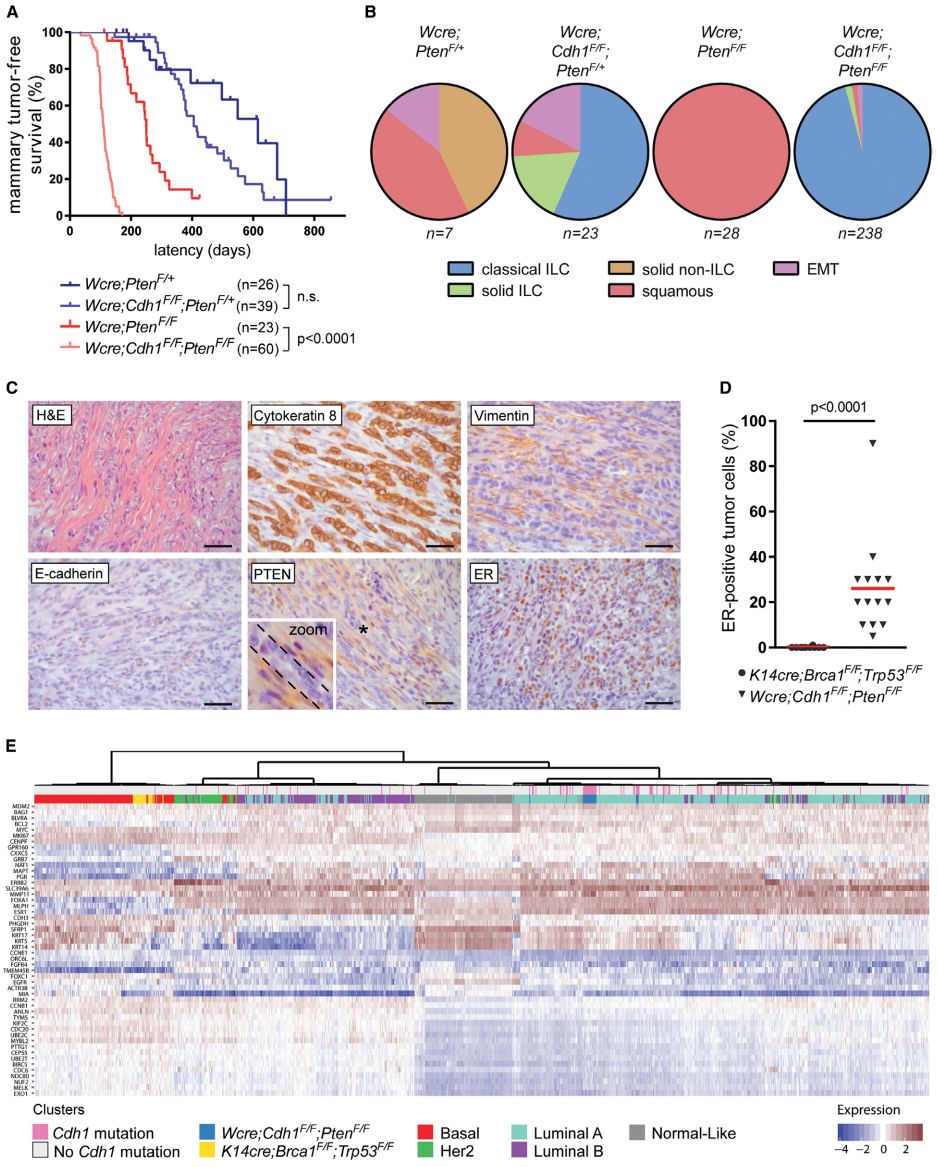

Figure 3. Somatic Inactivation of E-Cadherin and PTEN Induces Mammary Tumors that Closely Resemble Human CLC

(A) Mammary tumor-free survival plot of *Wcre;Pten*$^{F/+}$ (n = 26), *Wcre;Cdh1*$^{F/F}$*;Pten*$^{F/+}$ (n = 39), *Wcre;Pten*$^{F/F}$ (n = 23), and *Wcre;Cdh1*$^{F/F}$*;Pten*$^{F/F}$ (n = 60) mice. Latency is shown in days of age. n.s., not significant.

(B) Pie charts showing the distribution of mammary tumor phenotypes in *Wcre;Pten*$^{F/+}$ (n = 7), *Wcre;Cdh1*$^{F/F}$*;Pten*$^{F/+}$ (n = 23), *Wcre;Pten*$^{F/F}$ (n = 28), and *Wcre;Cdh1*$^{F/F}$*;Pten*$^{F/F}$ (n = 238) mice.

(C) Representative H&E staining and IHC of CK8, Vimentin, E-cadherin, PTEN, and ER in mammary tumors from 12-week-old *Wcre;Cdh1*$^{F/F}$*;Pten*$^{F/F}$ mice. Scale bars, 25 μm. The zoom of the asterisk-marked area reveals

PTEN-negative tumor cells flanked by PTEN-positive stromal cells.
(D) Quantification of ER-positive tumor cells detected by IHC of ER in *Brca1$^{\Delta/\Delta}$;Trp53$^{\Delta/\Delta}$* (n = 10) and *Cdh1$^{\Delta/\Delta}$;Pten$^{\Delta/\Delta}$* (n = 14) mammary tumors.
(E) Unsupervised hierarchical clustering of 956 human breast cancer samples, 22 *Brca1$^{\Delta/\Delta}$;Trp53$^{\Delta/\Delta}$* mammary tumor samples, and 20 *Cdh1$^{\Delta/\Delta}$;Pten$^{\Delta/\Delta}$* mCLC samples. Sidebars indicate tumor subtype according to PAM50 for the human breast tumors, genotypes for the mouse mammary tumors, and *Cdh1* mutation status for all tumors.

Inactivation of E-Cadherin and PTEN Drives Formation of Mammary Tumors that Closely Resemble Human CLC

To examine potential synergy between E-cadherin and PTEN loss in mammary tumorigenesis, we monitored tumor formation, as detected by palpation, in *Wcre;Pten$^{F/+}$*, *Wcre;Pten$^{F/F}$*, *Wcre;Cdh1$^{F/F}$;Pten$^{F/+}$*, and *Wcre;Cdh1$^{F/F}$;Pten$^{F/F}$* mice. In line with previous literature, female *Wcre;Pten$^{F/+}$* and *Wcre;Pten$^{F/F}$* mice developed heterozygous or homozygous mammary tumors, with median latencies of 615 and 250 days, respectively (Figure 3A) (Li et al., 2002). Additional inactivation of E-cadherin significantly decreased mammary tumor latency to 109 days of age in *Wcre;Cdh1$^{F/F}$;Pten$^{F/F}$* mice, demonstrating strong synergy between E-cadherin and PTEN loss in mammary tumorigenesis (Figure 3A). Interestingly, *Wcre;Cdh1$^{F/F}$;Pten$^{F/+}$* and *Wcre;Pten$^{F/+}$* female mice showed a similar tumor-free survival, indicating that complete loss of PTEN is required for malignant transformation of E-cadherin-deficient mammary epithelial cells (Figure 3A).

To analyze the mammary tumors for each genotype, mice were sacrificed when tumors reached 225 mm^2, except for *Wcre;Cdh1$^{F/F}$;Pten$^{F/F}$* mice, which were sacrificed after a median period of 101 days after tumor detection due to cumulative burden of multifocal tumors, abnormal locomotory behavior, or skin ulceration (both associated with infiltrating tumor cells in surrounding tissues) (Figure S3A). Mammary tumors from *Wcre; Pten$^{F/+}$*mice displayed diverse histological phenotypes, including solid carcinomas, squamous metaplastic carcinomas, and EMT-like tumors, while *Wcre; Pten$^{F/F}$* mice solely developed squamous metaplastic carcinomas (Figures 3B and S3A), suggesting that somatic PTEN loss, on its own, preferentially drives the development of this particular tumor type.

Notably, additional inactivation of E-cadherin completely shifted mammary tumor morphology. About half (57%) of mammary tumors in *Wcre;Cdh1$^{F/F}$;Pten$^{F/+}$* mice and nearly all (96%) tumors in *Wcre;Cdh1$^{F/F}$;Pten$^{F/F}$* mice displayed infiltrative patterns of single files of tumor cells into the surrounding stroma (Figures 3B and 3C). IHC staining of tumor sections confirmed the absence of E-cadherin and PTEN protein in CK8-marked tumor cells, whereas surrounding stromal cells retained PTEN expression (Figure 3C). Moreover, IHC staining revealed elevated levels of phosphorylated (p)-AKT, p-4ebp1,

and p-S6 in tumor cells, confirming the activation of PI3K signaling due to loss of PTEN (Figure S3B). Given that this phenotype comprises key characteristics of human CLC, we designated these tumors as mouse CLC (mCLC). Interestingly, mCLCs from *Wcre;Cdh1*$^{F/F}$*;Pten*$^{F/+}$ mice completely lost PTEN protein expression as analyzed by IHC, indicating that ILC formation requires complete loss of PTEN expression (Figure S3E). The remaining mammary tumors from *Wcre;Cdh1*$^{F/F}$*;Pten*$^{F/+}$ mice were classified as solid ILC, squamous metaplastic carcinomas, or EMT-like tumors that possibly developed due to incomplete loss of PTEN expression (Figure 3B).

Since the majority of human CLCs are estrogen receptor (ER) positive, we analyzed ER expression in mCLCs from *Wcre;Cdh1*$^{F/F}$*;Pten*$^{F/F}$ mice, revealing a mean of 26% ER-positive tumor cells (Figures 3C, 3D, and S3C). In contrast, a mean of only 0.1% ER-positive cells was observed in *Brca1*$^{\Delta/\Delta}$*;Trp53*$^{\Delta/\Delta}$ mouse mammary tumors, which are known to be ER negative (Liu et al., 2007). Also, the expression of *Esr1* mRNA, encoding ERα, was found to be increased in *Cdh1*$^{\Delta/\Delta}$*;Pten*$^{\Delta/\Delta}$ mCLCs, as compared to *Brca1*$^{\Delta/\Delta}$*;Trp53*$^{\Delta/\Delta}$ mouse mammary tumors (Figure S3F). Expression of *Esr1* mRNA was also observed in FACS (fluorescence-activated cell sorting)-sorted EpCAM (epithelial cell adhesion molecule)-positive tumor cells, confirming the ER positivity of tumor cells in mCLC (Figures S3C and S3F).

Based on their gene expression profiles, human CLCs are classified as luminal-A tumors (Ciriello et al., 2015, Iorfida et al., 2012). To assess the molecular subtype of mCLCs from *Wcre;Cdh1*$^{F/F}$*;Pten*$^{F/F}$ mice, hierarchical clustering of RNA-seq data from 956 human breast cancers and 42 mouse mammary tumors was performed using the PAM50 gene set, which allows classification of breast tumors into luminal, basal-like, HER2-positive and normal-like subgroups (Parker et al., 2009). Whereas the 22 *Brca1*$^{\Delta/\Delta}$*;Trp53*$^{\Delta/\Delta}$ mammary tumors clustered together with human basal-like breast cancers, all 20 *Cdh1*$^{\Delta/\Delta}$*;Pten*$^{\Delta/\Delta}$ mCLCs were classified as luminal-A tumors, indicating that these mouse tumors closely resemble the molecular subtype of human CLC (Figure 3E). In summary, the combined loss of E-cadherin and PTEN drives a rapid onset of mCLCs that recapitulate the morphology, ER positivity, and molecular subtype of human CLC.

Mammary Gland Reconstitution Exposes Slow and Linear Growth of De Novo mCLCs

Human CLCs are typically slow-growing tumors with a low-to-intermediate mitotic index. Unfortunately, mCLC growth kinetics could not be measured in *Wcre;Cdh1*$^{F/F}$*;Pten*$^{F/F}$ mice, which display multifocal tumor formation in all mammary glands. To assess the growth kinetics of mCLCs, we performed mammary gland reconstitutions by orthotopic transplantation of small fragments of tumor-free mammary gland tissue

from *Wcre;Cdh1$^{F/F}$;Pten$^{F/F}$* mice into cleared mammary fat pads of wild-type mice. In 82 out of 104 reconstituted mammary glands, a palpable tumor was detected after a median latency period of 102 days, which is similar to the median latency of 109 days in the spontaneous mouse model (Figure 4A). Since tumor development after mammary gland reconstitution occurred at a single location, it allowed reliable assessment of tumor size. Up to 250 days after tumor detection, which is more than twice the age the spontaneous mouse model reaches, a linear and slow growth rate was observed for all 82 tumors to an average size of only 8.6 mm^2 (Figures 4B, 4C, and S4A). These linear growth kinetics are unique for mouse tumors, which generally exhibit exponential tumor growth, and are very comparable to the slow growth kinetics of human CLC. The fact that mCLCs display constant and linear growth kinetics from the time of detection onward suggests that no additional mutations are required for CLC formation besides loss of E-cadherin and PTEN.

Interestingly, 17 out of 82 mCLCs showed a sudden transition from linear to exponential growth kinetics between 8 and 21 months after tumor detection (Figure 4D). These exponentially growing tumors displayed non-CLC phenotypes, including solid ILC and EMT-like tumors, which were also observed in a small fraction of the spontaneous tumors from *Wcre;Cdh1$^{F/F}$;Pten$^{F/F}$* mice (Figures 3B and S3B). The sudden and stochastic transition from linear to exponential growth kinetics suggests the acquisition of additional mutations in these tumors over time. Indeed, whole-exome sequencing of seven randomly selected exponentially growing tumors and 14 mCLCs revealed that all exponentially growing tumors harbored mutations in at least one cancer-related gene, while none of the mCLCs showed additional mutations (Figure 4E). Similarly, DNA copy-number variation (CNV) analysis showed that mCLCs displayed relatively stable genomic profiles, whereas exponentially growing tumors contained multiple DNA copy-number aberrations (Figures 4F and S4B).

In summary, we successfully developed a mammary gland reconstitution model for CLC, highlighting a linear growth rate of these tumors and indicating that combined E-cadherin and PTEN loss is sufficient and, thus, causal for CLC development.

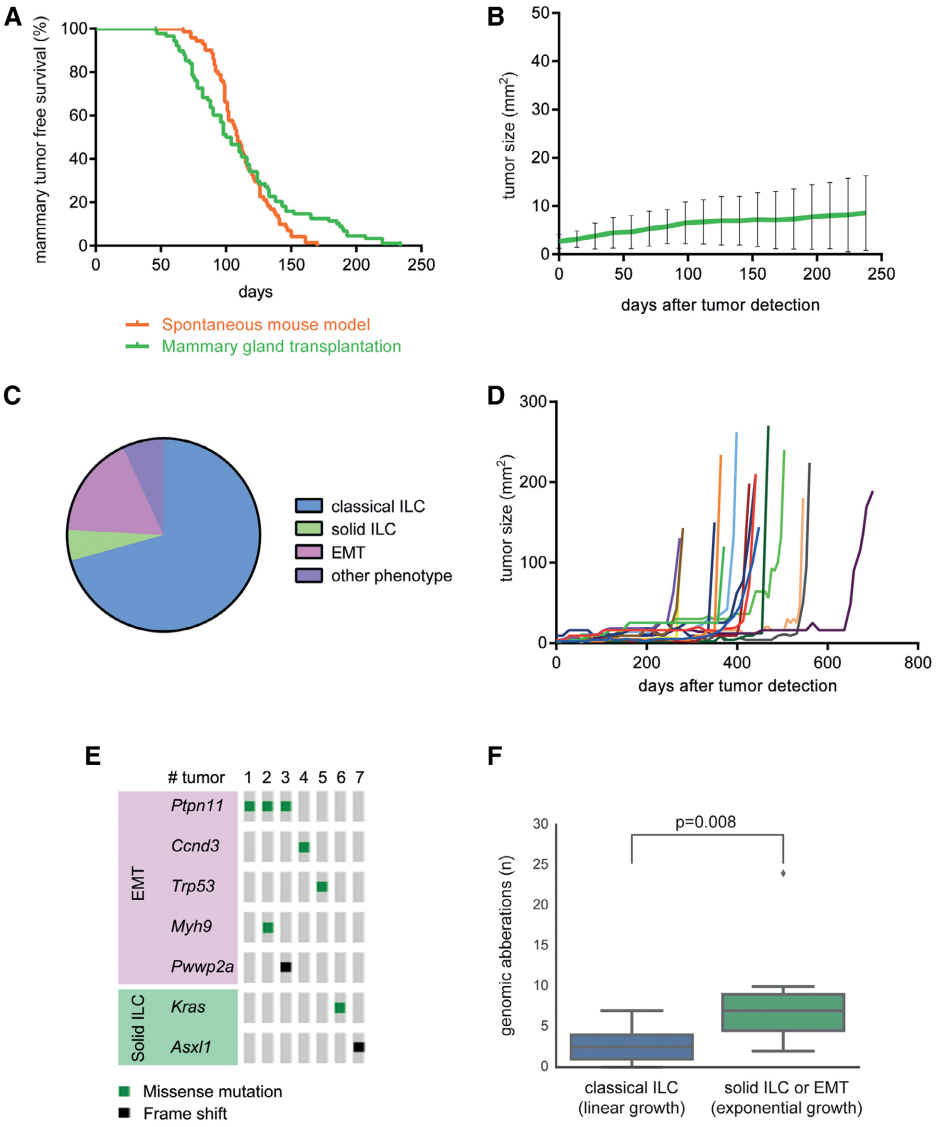

Figure 4. Mammary Gland Transplantation Reveals Linear Growth Kinetics of mCLCs

(A) Mammary-tumor-free survival in *Wcre;Cdh1*$^{F/F}$*;Pten*$^{F/F}$ mice and wild-type mice transplanted with small precancerous mammary gland fragments from *Wcre;Cdh1*$^{F/F}$*;Pten*$^{F/F}$ mice.

(B) Average size of tumors in mice transplanted with precancerous *Wcre;Cdh1*$^{F/F}$*;Pten*$^{F/F}$ mammary gland fragments (n = 82).

(C) Pie chart showing distribution of tumor phenotypes from mice transplanted with precancerous *Wcre;Cdh1*$^{F/F}$*;Pten*$^{F/F}$ mammary gland fragments (n = 58).

(D) A fraction (n = 17) of mice transplanted with precancerous *Wcre;Cdh1*$^{F/F}$*;Pten*$^{F/F}$ mammary gland fragments showed a sudden transition from linear to exponential growth 250–450 days after tumor onset.

(E) Overview of oncogenic mutations identified in exponentially growing solid ILCs and EMT tumors.
(F) Number of genomic aberrations in linear-growing mCLCs (n = 14) or exponential-growing solid ILCs and EMT tumors (n = 7).

Metastatic Spectrum of mCLCs Mimics that of Human CLC

Human CLC is characterized by its invasive and metastatic behavior. Similarly, mCLCs displayed tumor invasion, as detected by the examination of tumor sections, revealing irregular tumor edges with files of tumor cells invading surrounding tissues such as fat, muscle, and nerves (Figures 5A and 5B). In line with previous observations (Cheung et al., 2013), we observed a mixture of CK8 and cytokeratin-14 (CK14) double-positive tumor cells and CK14 single-positive tumor cells at the invasive front (Figure S5A). We also investigated metastatic behavior for each tumor genotype. In *Wcre;Pten$^{F/+}$* and *Wcre;Pten$^{F/F}$* mice, no microscopic metastases could be detected in any organ, possibly due to the presence of intact adherens junctions (Figure 5C). In contrast, microscopic or macroscopic metastases were observed in 34% and 5% of tumor-bearing *Wcre;Cdh1$^{F/F}$;Pten$^{F/+}$* and *Wcre;Cdh1$^{F/F}$;Pten$^{F/F}$* mice, respectively (Figure 5C). These metastases were detected at various distant sites that are also typical for human CLC, including lymph nodes, lungs, pleura, peritoneum, and abdominal viscera (Figures 5C and 5D). The distribution of the primary tumor phenotypes in mice that developed metastases was similar to the overall distribution, with the majority of primary tumors displaying an mCLC phenotype (Figures 3B and S5B). A plausible explanation for the lower number of metastases in *Wcre;Cdh1$^{F/F}$;Pten$^{F/F}$* mice lies in the fact that these mice were sacrificed at a relatively young age (median, 210 days), as compared to *Wcre;Cdh1$^{F/F}$;Pten$^{F/+}$* mice, which were sacrificed at a median age of 634 days (Figure S5C). Therefore, *Wcre;Cdh1$^{F/F}$;Pten$^{F/F}$* mice might have been too young at the time of sacrifice to permit detection of (slow-growing) metastases. This notion is supported by the fact that the *Wcre;Cdh1$^{F/F}$;Pten$^{F/F}$* mice with detectable metastases were the oldest of all mice analyzed (Figure S5D). However, no metastatic lesions were observed in lungs from ten aged mice that had been reconstituted with mammary gland tissue from *Wcre;Cdh1$^{F/F}$;Pten$^{F/F}$* mice as described earlier (Figure 4B). Therefore, it cannot be excluded that the late onset of tumor formation in *Wcre;Cdh1$^{F/F}$;Pten$^{F/+}$* mice might favor the development of distinct ILCs with increased metastatic capacity.

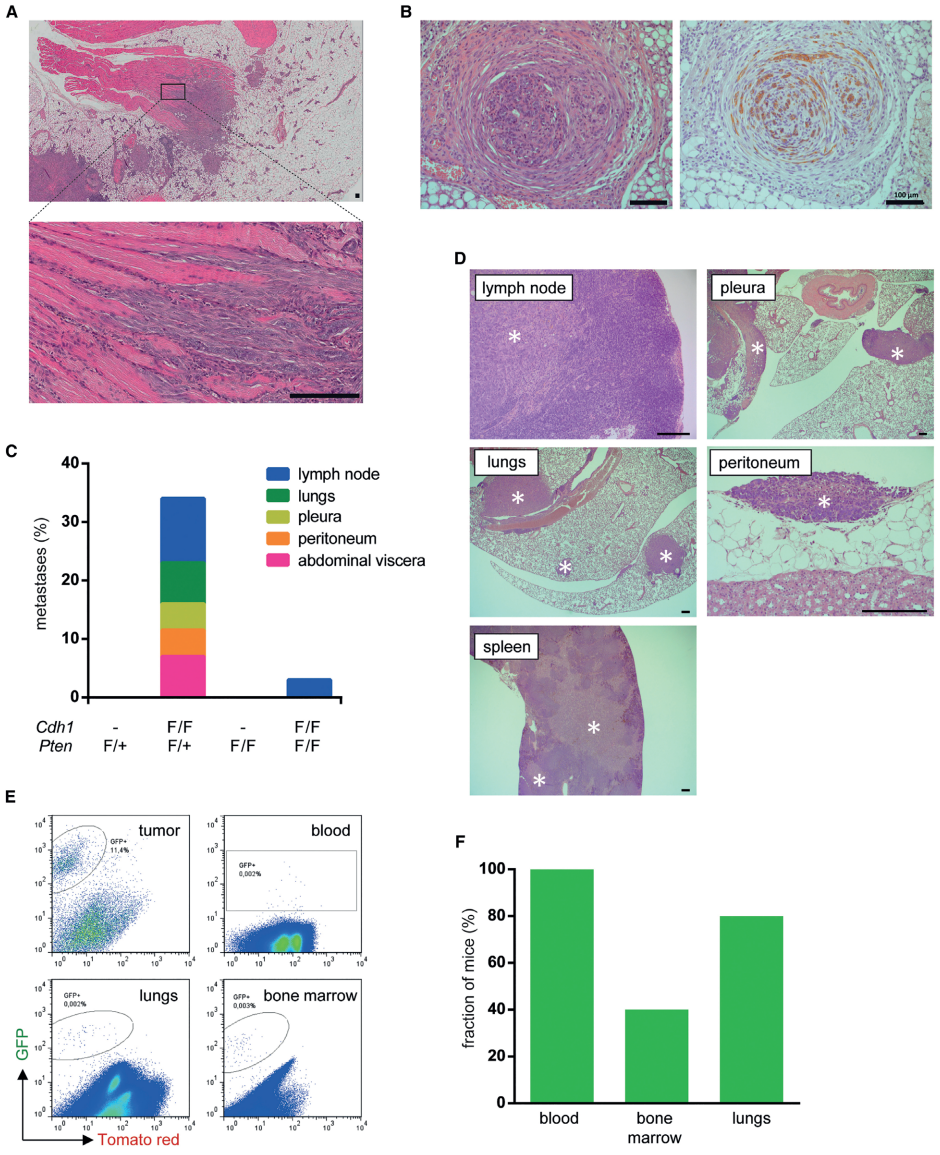

Figure 5. Metastatic Spectrum of mCLCs

(A and B) Representative H&E stainings revealing tumor cell invasion into surrounding muscular tissue (A) and nerve tissue (B) in mammary glands from 12-week-old *Wcre;Cdh1*$^{F/F}$*;Pten*$^{F/F}$ mice (scale bars, 100 µm).
(C) Incidence of distant metastases in *Wcre;Pten*$^{F/+}$ (n = 15), *Wcre;Cdh1*$^{F/F}$*;Pten*$^{F/+}$ (n = 32), *Wcre;Pten*$^{F/F}$ (n = 26), and *Wcre;Cdh1*$^{F/F}$*;Pten*$^{F/F}$ (n = 62) mice. Colors depict different metastatic sites in metastasis-bearing *Wcre;Cdh1*$^{F/F}$*;Pten*$^{F/+}$ (n = 11) and *Wcre;Cdh1*$^{F/F}$*;Pten*$^{F/F}$ (n = 3) mice.
(D) Representative H&E stainings of tumor infiltration (marked by asterisks) in lymph node, lung, pleura, peritoneum, and spleen. Scale bars, 200 µm.
(E) Representative FACS plots of GFP-sorted cells obtained from mammary tumors, blood, lungs, and bone

marrow of tumor-bearing *Wcre;Cdh1$^{F/F}$;Pten$^{F/F}$;mTmG* mice, revealing dissemination of GFP-marked tumor cells to distant organs.
(F) Fractions of *Wcre;Cdh1$^{F/F}$;Pten$^{F/F}$;mTmG* mice (n = 5) harboring GFP-marked tumor cells in indicated organs.

Next, we used FACS analysis to search for single mCLC cells in the circulation or in common sites of human CLC metastasis, such as bone marrow or lungs. To facilitate the identification of single tumor cells, we used *Wcre;Cdh1$^{F/F}$;Pten$^{F/F}$;mTmG* mice in which GFP expression marks *Wcre*-mediated loss of E-cadherin and PTEN (Muzumdar et al., 2007). IHC staining of mammary gland sections indeed confirmed the formation of GFP-positive mCLCs in *Wcre;Cdh1$^{F/F}$;Pten$^{F/F}$;mTmG* mice (Figure S5E). FACS analysis of primary tumor tissue from five *Wcre;Cdh1$^{F/F}$;Pten$^{F/F}$;mTmG* mice revealed 10%–15% GFP-positive cells, implying that the majority of cells in mCLC are non-tumor cells (Figure 5E). As expected, FACS analysis of blood samples revealed low numbers of circulating tumor cells (CTCs) in all *Wcre;Cdh1$^{F/F}$;Pten$^{F/F}$;mTmG* mice analyzed, suggesting that tumor cells are able to shed from the primary tumor and intravasate into the blood circulation (Figures 5E and 5F). Furthermore, low numbers of GFP-positive cells were detected in bone marrow and lung tissue, indicating infiltration of disseminated tumor cells into these organs (Figures 5E and 5F). The low number of GFP-marked tumor cells might underestimate the actual number of disseminated tumor cells, as the presence of Tomato and GFP double-positive CTCs in the blood revealed incomplete switching of the homozygous *mTmG* reporter alleles. Nevertheless, these results show that mCLCs exhibit an invasive and metastatic behavior that strongly resembles that of human CLC.

Early Stromal Recruitment in CLC

Histological and FACS analysis indicated mCLCs to contain a large proportion of non-tumor cells (Figures 3C and 5E). Therefore, we performed a detailed histological characterization of the tumor microenvironment of mCLCs and compared it to that of human CLCs. Besides H&E staining, we included Masson's trichrome staining to visualize collagen fibers, a major component of the extracellular matrix, and IHC stainings to detect fibroblasts (PDGFRβ), T cells as a major component of the adaptive immune system (CD3), and macrophages as a major component of the innate immune system (F4/80 or CD68).

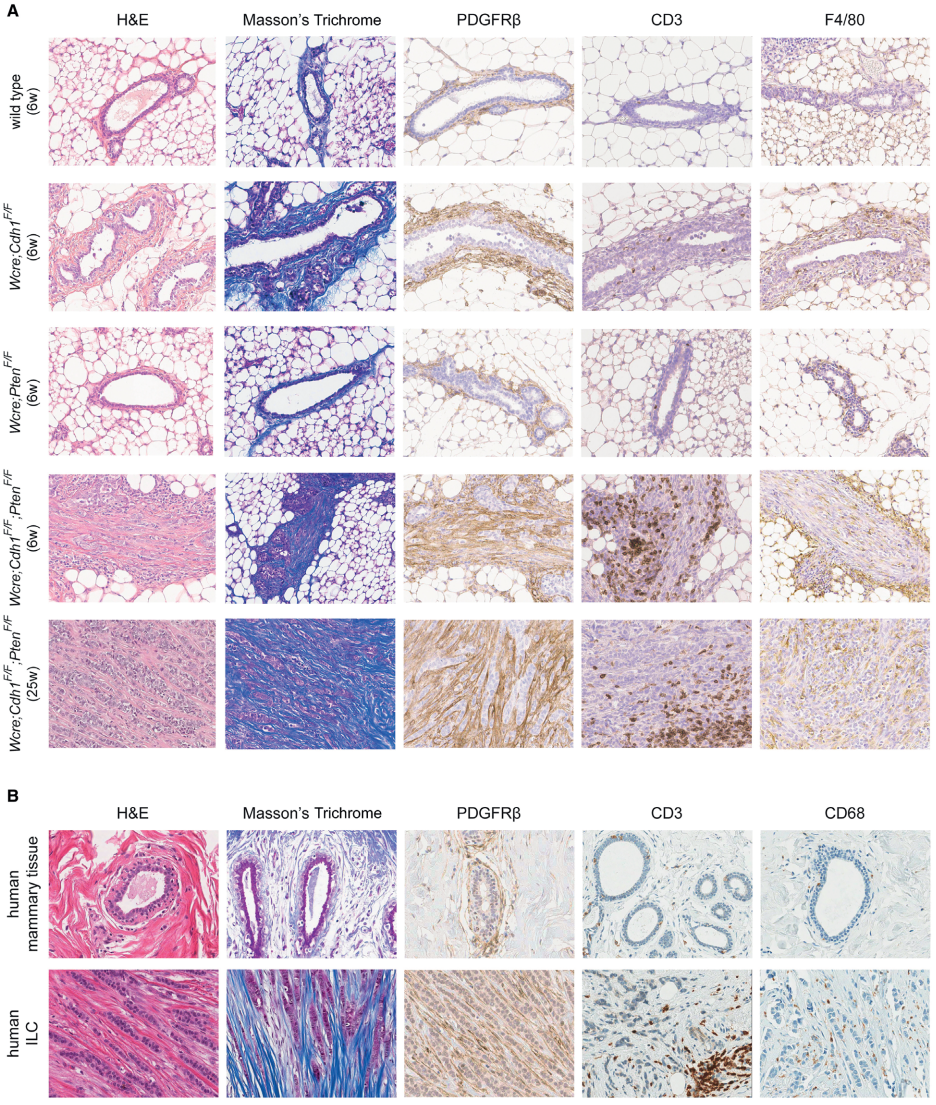

Figure 6. Early Stromal Recruitment in Mouse and Human CLC

(A and B) In (A), H&E and Masson's trichrome staining (revealing collagen) and IHC of PDGFRβ (fibroblasts), CD3 (T cells), and F4/80 (macrophages) in tumor-free mammary glands and mCLCs from wild-type, *Wcre;Cdh1*$^{F/F}$, *Wcre;Pten*$^{F/F}$, and *Wcre;Cdh1*$^{F/F}$*;Pten*$^{F/F}$ mice of indicated age were used to examine stromal compositions in each indicated genotype, which were subsequently compared to (B) the microenvironment of healthy human mammary glands and the tumor microenvironment of human CLCs.

We analyzed both early lesions and more advanced tumors in 6-week-old and 25-week-old wild-type, *Wcre;Cdh1*$^{F/F}$, *Wcre;Pten*$^{F/F}$, and *Wcre;Cdh1*$^{F/F}$*;Pten*$^{F/F}$ mice, respectively

(Figure 6A). In 6-week-old wild-type and *Wcre;Pten$^{F/F}$* mice (Figures 6A, S6A, and S6B) and 25-week-old wild-type mice (data not shown), mammary ducts were surrounded by a thin layer of blue-colored collagen fibers and PDGFRβ-positive fibroblasts, containing few CD3-positive T cells and F4/80-positive macrophages. In contrast, mammary ducts of both *Wcre;Cdh1$^{F/F}$* and *Wcre;Cdh1$^{F/F}$;Pten$^{F/F}$* mice clearly showed an altered microenvironment. In *Wcre;Cdh1$^{F/F}$* mammary glands, a relatively normal epithelial layer was surrounded by an thickened layer of collagen fibers and fibroblasts, showing slightly increased numbers of macrophages, but no notable changes in T cell numbers (Figure 6A). Even more profound changes in the microenvironment of mammary ducts were observed in *Wcre;Cdh1$^{F/F}$;Pten$^{F/F}$* mice. Early lesions of 6-week-old *Wcre;Cdh1$^{F/F}$;Pten$^{F/F}$* mice showed a clear increase in collagen and numbers of fibroblasts and displayed increased numbers of infiltrating macrophages and T cells, especially at the periphery (Figure 6A). Similar phenotypes were observed in more advanced tumors of 25-week-old *Wcre;Cdh1$^{F/F}$;Pten$^{F/F}$* mice, indicating that stromal recruitment is a continuous process with preservation of the composition (Figure 6A).

To investigate whether the stromal composition of mCLC resembles that of human CLC, we analyzed breast tissue samples from five healthy individuals and tumor tissue from 12 CLC patients. Analysis of normal breast tissue yielded similar results as those from wild-type mice, showing little collagen and low numbers of fibroblasts, T cells, or macrophages surrounding mammary ducts (Figure 6B). Similar to mCLCs, human CLCs showed abundant collagen fibers and fibroblasts, infiltrating macrophages, and increased numbers of T cells that were mainly located at the tumor periphery (Figure 6B). In summary, both human CLCs and mCLCs arising in *Wcre;Cdh1$^{F/F}$;Pten$^{F/F}$* mice are heterotypic tumors characterized by a rich stromal compartment consisting mainly of collagen and fibroblasts.

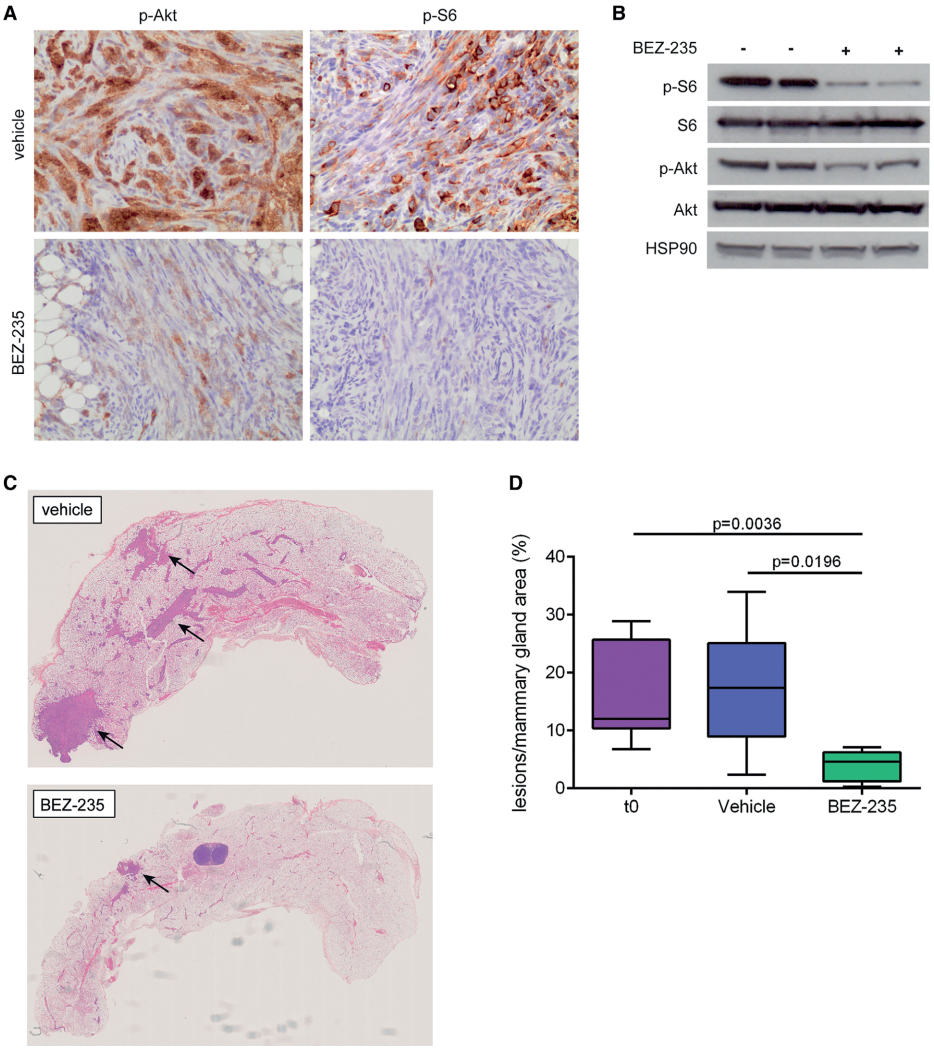

Figure 7. Inhibition of PI3K Signaling Has Antitumor Activity in *Wcre;Cdh1$^{F/F}$;Pten$^{F/F}$* Mice

(A) Representative IHC of p-AKT and p-S6, reflecting PI3K signaling activity in mCLCs from *Wcre;Cdh1$^{F/F}$;Pten$^{F/F}$* mice treated with either vehicle or BEZ235.

(B) Western blot analysis of p-AKT/AKT and p-S6/S6 expression, reflecting PI3K signaling activity in mCLCs from vehicle-treated and BEZ235-treated *Wcre;Cdh1$^{F/F}$;Pten$^{F/F}$* mice.

(C) H&E staining of mammary glands from *Wcre;Cdh1$^{F/F}$;Pten$^{F/F}$* mice treated with vehicle or BEZ235. Lesions are indicated by arrows.

(D) Quantification of lesion formation by measuring total lesion area over total mammary gland tissue area for vehicle-treated (n = 6) and BEZ235-treated (n = 6) *Wcre;Cdh1$^{F/F}$;Pten$^{F/F}$* littermates, compared to age-matched *Wcre;Cdh1$^{F/F}$;Pten$^{F/F}$* mice (n = 9) at start of treatment (t = 0).

Inhibition of PI3K Signaling Has Antitumor Activity in Wcre;Cdh1$^{F/F}$;Pten$^{F/F}$ Mice

As previously mentioned, the PI3K signaling pathway is frequently mutated in human ILC. In line with the role of PTEN as a negative regulator of PI3K signaling, CLCs from our *Wcre;Cdh1$^{F/F}$;Pten$^{F/F}$* mouse model showed activated PI3K signaling, as evidenced by elevated levels of p-AKT and p-S6 (Figure 7A). Given that improved treatments for human CLC are highly desirable, we asked whether the PI3K signaling pathway might be a potential therapeutic target for CLC. To this end, we performed a preclinical intervention study in *Wcre;Cdh1$^{F/F}$;Pten$^{F/F}$* female mice with the dual PI3K/mTOR (mammalian target of rapamycin) inhibitor BEZ235 (Liu et al., 2009). Eight-week-old littermates were treated with BEZ235 or vehicle for a period of 28 days. Target inhibition of the PI3K signaling pathway by BEZ235 was confirmed by IHC and western blotting, showing decreased phosphorylation of both AKT and S6 in CLCs from mice treated with BEZ235 (Figures 7A and 7B). As expected, vehicle-treated *Wcre;Cdh1$^{F/F}$;Pten$^{F/F}$* female mice showed, at the end of treatment, more and larger lesions than age-matched *Wcre;Cdh1$^{F/F}$;Pten$^{F/F}$* mice did at the start of treatment (t = 0) (Figures 7C and 7D). Significantly fewer and smaller CLC lesions were observed in the mammary glands of BEZ235-treated littermates compared to t = 0 and vehicle-treated *Wcre;Cdh1$^{F/F}$;Pten$^{F/F}$* mice, indicating that this PI3K/mTOR inhibitor strongly inhibited tumor formation in our mCLC model (Figures 7C and 7D). Together, these findings indicate that pharmacological inhibition of PI3K signaling may be a promising therapeutic strategy to target CLCs that harbor activating mutations in this pathway.

DISCUSSION

In this study, we show that concomitant inactivation of E-cadherin and PTEN leads to rapid formation of mouse mammary tumors that faithfully recapitulate the histopathology, molecular phenotype, ER status, growth kinetics, metastatic behavior, and tumor microenvironment of human CLC. Inactivating mutations of E-cadherin and PTEN co-occur in a substantial fraction (13%) of human ILCs (Ciriello et al., 2015). In line with this, our data revealed potent synergism and causality between E-cadherin and PTEN inactivation in CLC formation. Previously, we reported that inactivation of E-cadherin and P53 in mammary epithelium results in the development of pleomorphic ILC, a relatively rare subtype of ILC (Derksen et al., 2006, Derksen et al., 2011). In contrast, inactivation of PTEN alters the tumor outcome of E-cadherin-deficient cells toward CLC, which is the most common subtype of ILC (Iorfida et al., 2012). Although E-cadherin inactivation alone is insufficient to induce tumor formation (Boussadia

et al., 2002, Derksen et al., 2006, Derksen et al., 2011), it appears to be required for ILC formation by dictating tumor outcome of P53- and PTEN-deficient mammary epithelial cells toward pleomorphic ILC and CLC, respectively. Thus, besides being recognized as a hallmark of ILC (Zschiesche et al., 1997), E-cadherin inactivation is also required for ILC formation.

In apparent contrast to its tumor-suppressor role, E-cadherin inactivation limits mammary epithelial cell survival in vivo as E-cadherin-deficient luminal epithelial cells were found to accumulate in the lumen of mammary ducts and undergo apoptosis, which is most likely due to reduced junctional integrity caused by E-cadherin loss (Shamir et al., 2014). Previously, E-cadherin inactivation in the mammary gland was found to limit the survival of alveolar cells during the onset of lactation (Boussadia et al., 2002), supporting a role for E-cadherin in maintaining the survival of luminal mammary epithelial cells. E-cadherin-deficient mammary epithelium was also unable to expand in vitro and required concomitant inactivation of PTEN for outgrowth and invasion. PTEN inactivation also enabled the survival of E-cadherin-deficient mammary epithelial cells in vivo, permitting the formation of CLC. Importantly, as tumor onset in female *Wcre;Cdh1$^{F/F}$;Pten$^{F/F}$* mice was extremely rapid, and no additional mutations were detected in the ensuing mCLCs, the combined inactivation of E-cadherin and PTEN appears to be sufficient and, thus, causal for CLC formation.

PTEN is an important negative regulator of the PI3K signaling pathway, which controls cell survival (Cully et al., 2006). It is, therefore, likely that activation of PI3K signaling due to loss of PTEN promotes the survival of E-cadherin-deficient mammary epithelial cells and subsequent formation of CLC. Indeed, mCLCs from our *Wcre;Cdh1$^{F/F}$;Pten$^{F/F}$* mouse model showed activated PI3K signaling, as evidenced by expression of p-AKT and p-S6. Also, human ILCs were found to show frequent activation of PI3K signaling, as evidenced by increased AKT phosphorylation, reduced PTEN expression, and a high incidence of somatic mutations leading to PI3K pathway activation (Ciriello et al., 2015). Together, these data suggest that PI3K pathway inhibitors might effectively target CLC. In line with this, mCLC formation in female *Wcre;Cdh1$^{F/F}$;Pten$^{F/F}$* mice was significantly decreased by treatment with the dual PI3K/mTOR inhibitor BEZ235, indicating that the PI3K signaling pathway is an important Achilles' heel of CLC. At present, BEZ235 is under evaluation in phase I/II clinical trials (Bendell et al., 2015), and future studies are needed to investigate its efficacy in patients with CLC. However, it should be noted that antitumoral efficacy of PI3K pathway inhibitors might be reduced, in case CLCs acquire additional activating mutations in oncoproteins, such as KRAS, or

loss-of-function mutations in tumor suppressors, such as PTPN11/SHP2 and p53, which we identified to alter tumor outcome and growth kinetics of mCLCs.

Other strategies to target CLC might involve targeting the tumor microenvironment, which can promote growth, metastasis, and therapy resistance of breast cancer (Boelens et al., 2014, Giussani et al., 2015, Unsworth et al., 2014). Furthermore, the massive deposition of collagen in the tumor microenvironment of both mouse and human CLC suggests that collagen production is important for CLC development and progression. Collagen has been implicated in the induction of tumor cell invasion, as it was found to accumulate at invasive edges in breast tumors (Egeblad et al., 2010, Provenzano et al., 2006) and to induce in vitro invasion of cultured breast tumor cells (Nguyen-Ngoc et al., 2012). Similarly, tumor cells in mCLCs align with collagen as they invade the surrounding tissue. Both mouse and human CLC showed massive infiltration of fibroblasts, which are, in general, the main source of collagen deposition. Future studies will be required to investigate the importance of these cancer-associated fibroblasts (CAFs) for mCLC development and progression and whether targeting CAFs might provide a useful strategy for treatment of human CLC.

In conclusion, in this study we presented concomitant inactivation of E-cadherin and PTEN in mammary epithelium to drive the formation of mCLC, thus developing a pertinent mouse model for human CLC. This mouse model provides a powerful in vivo tool to develop novel therapeutic strategies for CLC patients, which may extend the relative limited treatment options that are currently available in the clinic.

EXPERIMENTAL PROCEDURES

Generation of Mice

We intercrossed *Wcre;Cdh1*$^{F/F}$ mice (Derksen et al., 2011, Derksen et al., 2006) with *Pten*$^{F/F}$ mice (Ma et al., 2005) and *mTmG* reporter mice (Muzumdar et al., 2007). Mice were bred onto an FVB/N background and genotyped as described previously (Derksen et al., 2006, Ma et al., 2005); (Muzumdar et al., 2007). All animal experiments were approved by the Animal Ethical Committee and were conducted in compliance with the Netherlands Cancer Institute and Dutch Animal Welfare guidelines.

Isolation of Primary Mammary Epithelium for Organoid Generation

Purified primary mammary epithelial fragments were obtained from isolated mammary glands by mechanical disruption, collagenase/trypsin digestion, and differential

centrifugation to generate organoids as previously described (Ewald et al., 2008). For additional details, see the Supplemental Information.

Immunoblotting, IF, and Histopathology

Immunoblotting, IF, and histopathological analysis was performed as described in the Supplemental Information.

Mammary Gland Reconstitution

Mammary gland reconstitutions were performed based on previously described mouse mammary epithelial cell transplantation (Evers et al., 2010). In brief, the fourth mammary glands of 18- to 21-day-old wild-type or *mTmG* mice on FVB/N background were cleared by surgical removal of the epithelium-containing part, including the lymph node, and were engrafted with small fragments (1-2 mm in diameter) of mammary gland tissue from 5- to 6-week-old *Wcre;Cdh1*$^{F/F}$*;Pten*$^{F/F}$ mice. Transplanted mice were checked biweekly for the development of tumors.

Genomic Analysis

RNA sequencing, whole-exome sequencing, and CNV analysis was performed as described in the Supplemental Information.

Flow Cytometry

Blood samples were collected in tubes containing heparin. Tumors and lungs were mechanically chopped using a McIlwain tissue chopper (Mickle Laboratory Engineering), followed by digestion for 1 hr at 37°C in 3 mg/ml collagenase type A (Roche) and 25 µg/ml DNase (Sigma-Aldrich) in serum-free DMEM medium. Enzyme activity was neutralized by the addition of cold DMEM/10% fetal bovine serum (FBS), and suspensions were dispersed through a 70-µm cell strainer. Bone marrow was isolated through the flushing of two femurs using PBS. All single-cell suspensions were treated with erythrocyte lysis buffer (0.15 M NH_4Cl, 10 mM $KHCO_3$, 0.5 M EDTA) and collected in PBS + 1% BSA. DAPI (1:20) was added to exclude dead cells. GFP-positive cells were analyzed using a Beckman Coulter CyAn ADP flow cytometer and FlowJo software.

BEZ235 Intervention Study

Eight-week-old littermates were orally dosed on a daily basis with 30 mg/kg BEZ235 dissolved in 10% N-methyl-2-pyrrolidone/90% PEG 400 (polyethylene glycol 400) (Sigma-Aldrich) or vehicle for a period of 28 days. Two hours after the last dosing, mice

were sacrificed, and mammary glands were harvested for further analysis. Antitumor activity was assessed by calculating the ratio between the sum of all CLC regions and the total mammary gland area using ImageJ.

Statistics

The following statistics were used for the indicated figures: for Figures 1C, 1E, 2D, S2C, and S2D, an unpaired t test was used; for Figures 3A and S3A, we used a log-rank Mantel-Cox test; for Figure 3D, a Mann-Whitney test was used; for Figure S3C, differential expression was assessed using limma (Ritchie et al., 2015); and a one-tailed Mann-Whitney U test was used for Figure 4E. For Figure 7D, a paired t test was performed on these ratios between BEZ235- and vehicle-treated littermates.

AUTHOR CONTRIBUTIONS

M.C.B., M.N., S.K., R.v.A., and J.J. conceived experiments and analyzed data. M.C.B., M.N., S.K., E.S., N.B., A.L.Z., J.R.d.R., E.W., and E.v.d.B. conducted experiments. L.W. provided expertise and feedback. M.C.B., M.N., and J.J. wrote the manuscript.

ACKNOWLEDGMENTS

We are grateful to Anne Paulien Drenth, Ute Boon, and Renske de Korte-Grimmerink for help with the mammary gland reconstitutions and to the NKI Molecular Pathology & Biobanking Facility for supplying human tumor material and lab support. We thank the NKI animal facility, animal pathology facility, flow cytometry facility, and genomics core facility for technical support. This work was supported by grants from the Dutch Cancer Society (NKI 2015-7589); the Netherlands Organization for Scientific Research ([VENI 016156012, NGI-Zenith 93512009, and VICI 91814643], Cancer Genomics Netherlands [CGCNL], Cancer Systems Biology Center [CSBC], and a National Roadmap grant for the Mouse Clinic for Cancer and Aging research [MCCA]); the European Union Seventh Framework Programme (EurocanPlatform project 260791 and Infrafrontier-I3 project 312325); and the European Research Council (ERC Synergy project CombatCancer).

REFERENCES

Bendell et al., 2015

J.C. Bendell, C. Kurkjian, J.R. Infante, T.M. Bauer, H.A. Burris 3rd, F.A. Greco, K.C. Shih, D.S. Thompson, C.M. Lane, L.H. Finney, S.F. JonesA phase 1 study of the sachet formulation of the oral dual PI3K/mTOR inhibitor BEZ235 given twice daily (BID) in patients with advanced solid tumors

Invest. New Drugs, 33 (2015), pp. 463-471

Boelens et al., 2014

M.C. Boelens, T.J. Wu, B.Y. Nabet, B. Xu, Y. Qiu, T. Yoon, D.J. Azzam, C. Twyman-Saint Victor, B.Z. Wiemann, H. Ishwaran, *et al.*Exosome transfer from stromal to breast cancer cells regulates therapy resistance pathways

Cell, 159 (2014), pp. 499-513

Boussadia et al., 2002

O. Boussadia, S. Kutsch, A. Hierholzer, V. Delmas, R. KemlerE-cadherin is a survival factor for the lactating mouse mammary gland

Mech. Dev., 115 (2002), pp. 53-62

Buttitta et al., 2006

F. Buttitta, L. Felicioni, F. Barassi, C. Martella, D. Paolizzi, G. Fresu, S. Salvatore, F. Cuccurullo, A. Mezzetti, D. Campani, A. MarchettiPIK3CA mutation and histological type in breast carcinoma: high frequency of mutations in lobular carcinoma

J. Pathol., 208 (2006), pp. 350-355

Cheung et al., 2013

K.J. Cheung, E. Gabrielson, Z. Werb, A.J. EwaldCollective invasion in breast cancer requires a conserved basal epithelial program

Cell, 155 (2013), pp. 1639-1651

Ciriello et al., 2015

G. Ciriello, M.L. Gatza, A.H. Beck, M.D. Wilkerson, S.K. Rhie, A. Pastore, H. Zhang, M. McLellan, C. Yau, C. Kandoth, *et al.*, TCGA Research NetworkComprehensive molecular portraits of invasive lobular breast cancer

Cell, 163 (2015), pp. 506-519

Cully et al., 2006

M. Cully, H. You, A.J. Levine, T.W. MakBeyond PTEN mutations: the PI3K pathway as an integrator of multiple inputs during tumorigenesis

Nat. Rev. Cancer, 6 (2006), pp. 184-192

Derksen et al., 2006

P.W.B. Derksen, X. Liu, F. Saridin, H. van der Gulden, J. Zevenhoven, B. Evers, J.R. van Beijnum, A.W. Griffioen, J. Vink, P. Krimpenfort, *et al.*Somatic inactivation of E-cadherin and p53 in mice leads to metastatic lobular mammary carcinoma through induction of anoikis resistance and angiogenesis

Cancer Cell, 10 (2006), pp. 437-449

Derksen et al., 2011
P.W.B. Derksen, T.M. Braumuller, E. van der Burg, M. Hornsveld, E. Mesman, J. Wesseling, P. Krimpenfort, J. JonkersMammary-specific inactivation of E-cadherin and p53 impairs functional gland development and leads to pleomorphic invasive lobular carcinoma in mice
Dis. Model. Mech., 4 (2011), pp. 347-358

Egeblad et al., 2010
M. Egeblad, E.S. Nakasone, Z. WerbTumors as organs: complex tissues that interface with the entire organism
Dev. Cell, 18 (2010), pp. 884-901

Evers et al., 2010
B. Evers, E.N. Speksnijder, E. Schut, M. Ciampricotti, M.J. Smalley, P.W.B. Derksen, J. Jonkers, K.E. de VisserA tissue reconstitution model to study cancer cell-intrinsic and -extrinsic factors in mammary tumourigenesis
J. Pathol., 220 (2010), pp. 34-44

Ewald et al., 2008
A.J. Ewald, A. Brenot, M. Duong, B.S. Chan, Z. WerbCollective epithelial migration and cell rearrangements drive mammary branching morphogenesis
Dev. Cell, 14 (2008), pp. 570-581

Giussani et al., 2015
M. Giussani, G. Merlino, V. Cappelletti, E. Tagliabue, M.G. DaidoneTumor-extracellular matrix interactions: Identification of tools associated with breast cancer progression
Semin. Cancer Biol., 35 (2015), pp. 3-10

Houssami et al., 2003
N. Houssami, L. Irwig, J.M. Simpson, M. McKessar, S. Blome, J. NoakesThe contribution of work-up or additional views to the accuracy of diagnostic mammography
Breast, 12 (2003), pp. 270-275

Iorfida et al., 2012
M. Iorfida, E. Maiorano, E. Orvieto, P. Maisonneuve, L. Bottiglieri, N. Rotmensz, E. Montagna, S. Dellapasqua, P. Veronesi, V. Galimberti, *et al.*Invasive lobular breast cancer: subtypes and outcome
Breast Cancer Res. Treat., 133 (2012), pp. 713-723

Li et al., 2002
G. Li, G.W. Robinson, R. Lesche, H. Martinez-Diaz, Z. Jiang, N. Rozengurt, K.-U. Wagner, D.-C. Wu, T.F. Lane, X. Liu, *et al.*Conditional loss of PTEN leads to precocious development and neoplasia in the mammary gland
Development, 129 (2002), pp. 4159-4170

Li et al., 2003
C.I. Li, K.E. Malone, P.L. Porter, N.S. Weiss, M.-T.C. Tang, J.R. DalingReproductive and anthropometric factors in relation to the risk of lobular and ductal breast carcinoma among women 65-79 years of age
Int. J. Cancer, 107 (2003), pp. 647-651

Liu et al., 2007

X. Liu, H. Holstege, H. van der Gulden, M. Treur-Mulder, J. Zevenhoven, A. Velds, R.M. Kerkhoven, M.H. van Vliet, L.F.A. Wessels, J.L. Peterse, *et al.*Somatic loss of BRCA1 and p53 in mice induces mammary tumors with features of human BRCA1-mutated basal-like breast cancer

Proc. Natl. Acad. Sci. USA, 104 (2007), pp. 12111-12116

Liu et al., 2009

T.-J. Liu, D. Koul, T. LaFortune, N. Tiao, R.J. Shen, S.-M. Maira, C. Garcia-Echevrria, W.K.A. YungNVP-BEZ235, a novel dual phosphatidylinositol 3-kinase/mammalian target of rapamycin inhibitor, elicits multifaceted antitumor activities in human gliomas

Mol. Cancer Ther., 8 (2009), pp. 2204-2210

Ma et al., 2005

X. Ma, A.C. Ziel-van der Made, B. Autar, H.A. van der Korput, M. Vermeij, P. van Duijn, K.B. Cleutjens, R. de Krijger, P. Krimpenfort, A. Berns, *et al.*Targeted biallelic inactivation of Pten in the mouse prostate leads to prostate cancer accompanied by increased epithelial cell proliferation but not by reduced apoptosis

Cancer Res., 65 (2005), pp. 5730-5739

Michaut et al., 2016

M. Michaut, S.-F. Chin, I. Majewski, T.M. Severson, T. Bismeijer, L. de Koning, J.K. Peeters, P.C. Schouten, O.M. Rueda, A.J. Bosma, *et al.*Integration of genomic, transcriptomic and proteomic data identifies two biologically distinct subtypes of invasive lobular breast cancer

Sci. Rep., 6 (2016), p. 18517

Michelucci et al., 2009

A. Michelucci, C. Di Cristofano, A. Lami, P. Collecchi, A. Caligo, N. Decarli, M. Leopizzi, P. Aretini, G. Bertacca, R.P. Porta, *et al.*PIK3CA in breast carcinoma: a mutational analysis of sporadic and hereditary cases

Diagn. Mol. Pathol., 18 (2009), pp. 200-205

Moll et al., 1993

R. Moll, M. Mitze, U.H. Frixen, W. BirchmeierDifferential loss of E-cadherin expression in infiltrating ductal and lobular breast carcinomas

Am. J. Pathol., 143 (1993), pp. 1731-1742

Muzumdar et al., 2007

M.D. Muzumdar, B. Tasic, K. Miyamichi, L. Li, L. LuoA global double-fluorescent Cre reporter mouse

Genesis, 45 (2007), pp. 593-605

Nguyen-Ngoc et al., 2012

K.-V. Nguyen-Ngoc, K.J. Cheung, A. Brenot, E.R. Shamir, R.S. Gray, W.C. Hines, P. Yaswen, Z. Werb, A.J. EwaldECM microenvironment regulates collective migration and local dissemination in normal and malignant mammary epithelium

Proc. Natl. Acad. Sci. USA, 109 (2012), pp. E2595-E2604

Parker et al., 2009
J.S. Parker, M. Mullins, M.C.U. Cheang, S. Leung, D. Voduc, T. Vickery, S. Davies, C. Fauron, X. He, Z. Hu, *et al.*Supervised risk predictor of breast cancer based on intrinsic subtypes
J. Clin. Oncol., 27 (2009), pp. 1160-1167

Pestalozzi et al., 2008
B.C. Pestalozzi, D. Zahrieh, E. Mallon, B.A. Gusterson, K.N. Price, R.D. Gelber, S.B. Holmberg, J. Lindtner, R. Snyder, B. Thürlimann, *et al.*, International Breast Cancer Study GroupDistinct clinical and prognostic features of infiltrating lobular carcinoma of the breast: combined results of 15 International Breast Cancer Study Group clinical trials
J. Clin. Oncol., 26 (2008), pp. 3006-3014

Provenzano et al., 2006
P.P. Provenzano, K.W. Eliceiri, J.M. Campbell, D.R. Inman, J.G. White, P.J. KeelyCollagen reorganization at the tumor-stromal interface facilitates local invasion
BMC Med., 4 (2006), p. 38

Ritchie et al., 2015
M.E. Ritchie, B. Phipson, D. Wu, Y. Hu, C.W. Law, W. Shi, G.K. Smythlimma powers differential expression analyses for RNA-sequencing and microarray studies
Nucleic Acids Res., 43 (2015), p. e47

Shamir et al., 2014
E.R. Shamir, E. Pappalardo, D.M. Jorgens, K. Coutinho, W.-T. Tsai, K. Aziz, M. Auer, P.T. Tran, J.S. Bader, A.J. EwaldTwist1-induced dissemination preserves epithelial identity and requires E-cadherin
J. Cell Biol., 204 (2014), pp. 839-856

Unsworth et al., 2014
A. Unsworth, R. Anderson, K. BrittStromal fibroblasts and the immune microenvironment: partners in mammary gland biology and pathology?
J. Mammary Gland Biol. Neoplasia, 19 (2014), pp. 169-182

Zschiesche et al., 1997
W. Zschiesche, I. Schönborn, J. Behrens, K. Herrenknecht, F. Hartveit, P. Lilleng, W. BirchmeierExpression of E-cadherin and catenins in invasive mammary carcinomas
Anticancer Res., 17 (1B) (1997), pp. 561-567

SUPPLEMENTAL FIGURES

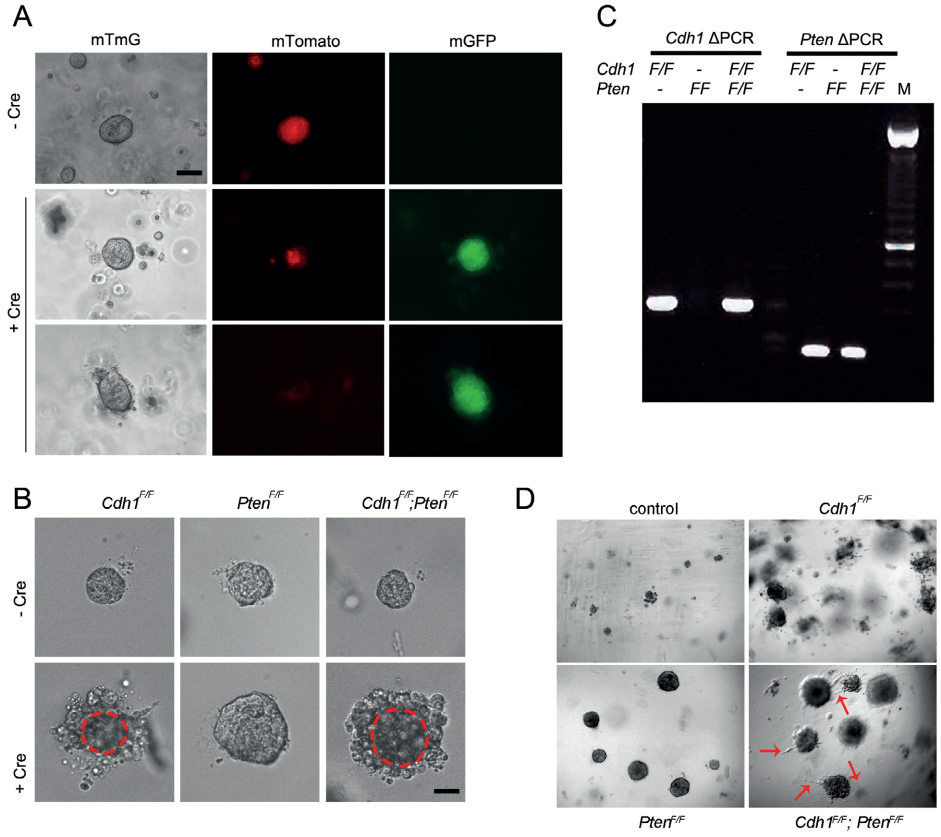

Supplemental Figure S1. Analysis of Cre recombinase activity in AdCre transduced mammary organoids

(A) Fluorescent analysis of untransduced and AdCre transduced mTmG organoids to asses organoid transduction efficiency as displayed by conversion of RFP into GFP-driven fluorescence at 7 days of organoid culture. Bar=50µm. (B) Representative images of untransduced or AdCre transduced *Cdh1*$^{F/F}$, *Pten*$^{F/F}$ and *Cdh1*$^{F/F}$;*Pten*$^{F/F}$ mammary organoids at 7 days of organoid culture. Bar=50µm. (C) PCR analysis of recombined floxed *Cdh1* and *Pten* alleles (ΔPCR) in AdCre transduced *Cdh1*$^{F/F}$, *Pten*$^{F/F}$ and *Cdh1*$^{F/F}$;*Pten*$^{F/F}$ mammary organoids. (D) Representative overview of untransduced and AdCre transduced *Cdh1*$^{F/F}$, *Pten*$^{F/F}$ and *Cdh1*$^{F/F}$;*Pten*$^{F/F}$ mammary organoids at day 15 of organoid culture, one day after renewal of culture medium.

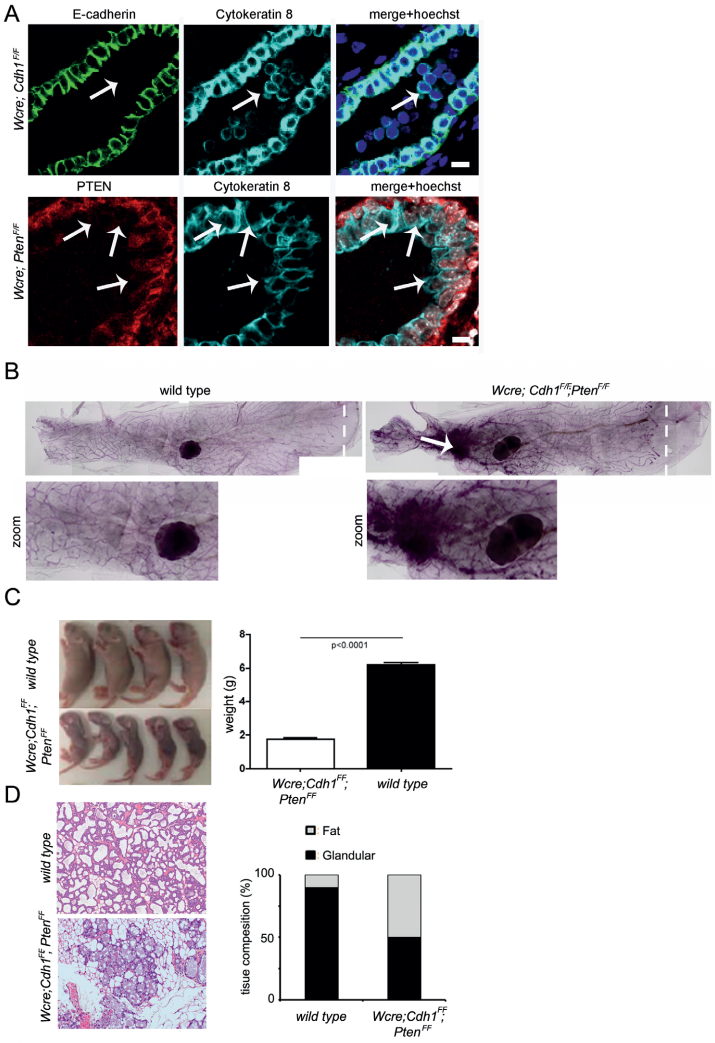

Supplemental Figure S2. Analysis of somatic inactivation of E-cadherin or PTEN in mouse mammary epithelium

(A) Immunofluorescence analyses of CK8, E-cadherin and PTEN in mammary epithelial tissue sections of 6-week-old *Wcre;Cdh1*$^{F/F}$ and *Wcre;Pten*$^{F/F}$ mice. Arrows highlight accumulation of E-cadherin deficient CK8-positive luminal cells in the duct of the mammary epithelium of *Wcre;Cdh1*$^{F/F}$ mice in contrast to PTEN-inactivated mammary luminal cells in *Wcre;Pten*$^{F/F}$ mice. Bar=25µm. (B) Comparison of mammary epithelial outgrowth by Carmine-alum whole-mount staining of mammary glands from 8-week-old wildtype (n=9) and *Wcre;Cdh1*$^{F/F}$*;Pten*$^{F/F}$ (n=9) mice. The dashed lines mark the leading edge and the arrow highlights lesion formation. (C) Size and weight of 6-day-old pups nursed by wildtype and *Wcre;Cdh1*$^{F/F}$*;Pten*$^{F/F}$ dams, showing impaired growth of pups nursed by *Wcre;Cdh1*$^{F/F}$*;Pten*$^{F/F}$ dams. (D) Comparison of mammary gland development during pregnancy by H&E staining of wildtype and *Wcre;Cdh1*$^{F/F}$*;Pten*$^{F/F}$ pregnant mice as quantified by measuring glandular and fat tissue.

A

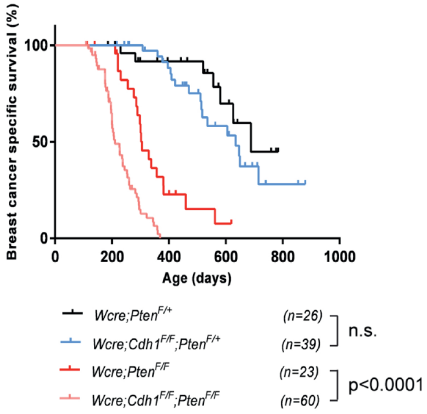
Breast cancer specific survival (%)
100
50
0
0
200
400
600
800
1000
Age (days)
Wcre;Pten F/+ (n=26)
Wcre;Cdh1 F/F ;Pten F/+ (n=39)
n.s.
Wcre;Pten F/F (n=23)
Wcre;Cdh1 F/F ;Pten F/F (n=60)
p<0.0001

B

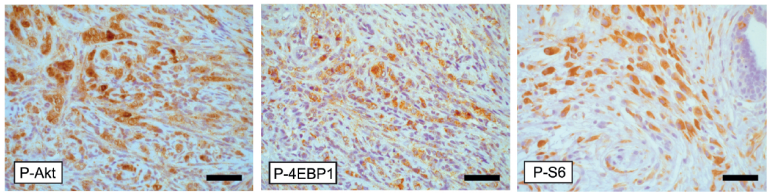
P-Akt
P-4EBP1
P-S6

C

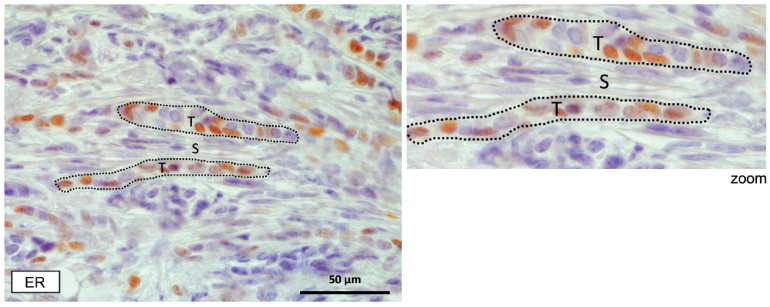
T
S
T
ER
50 µm
T
S
T
zoom

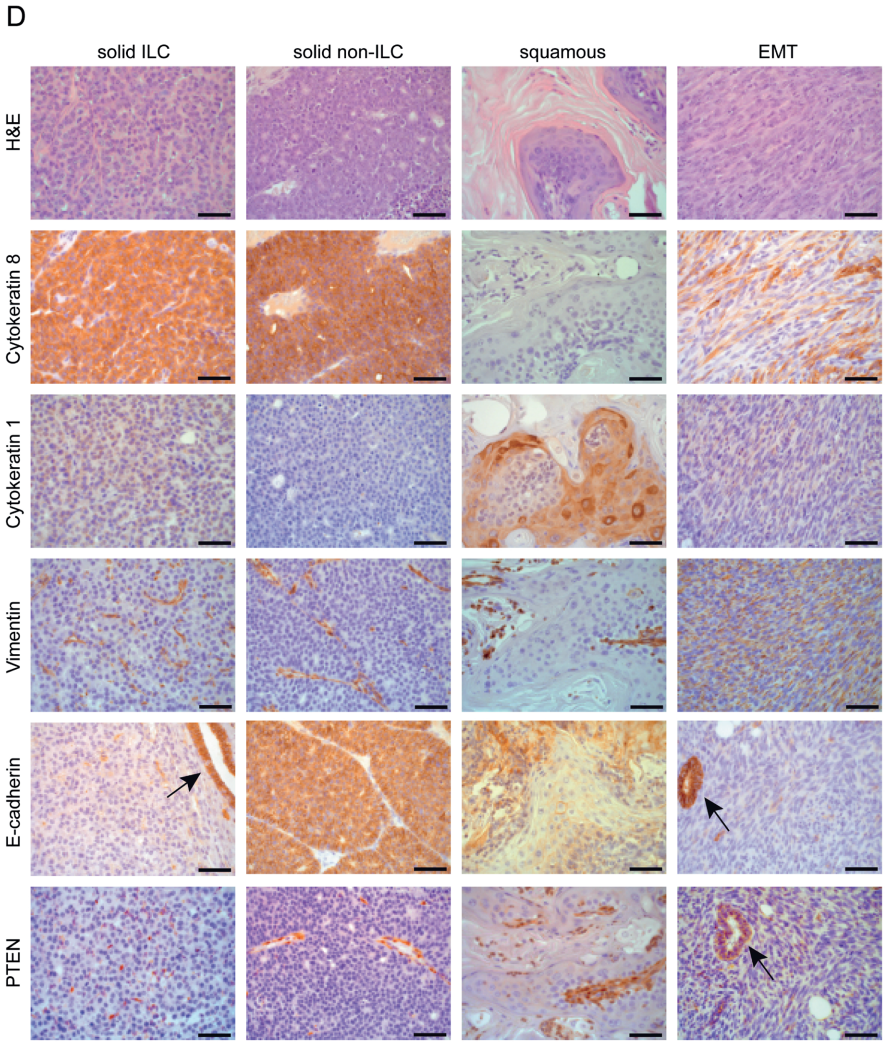
D
solid ILC
solid non-ILC
squamous
EMT
H&E
Cytokeratin 8
Cytokeratin 1
Vimentin
E-cadherin
PTEN

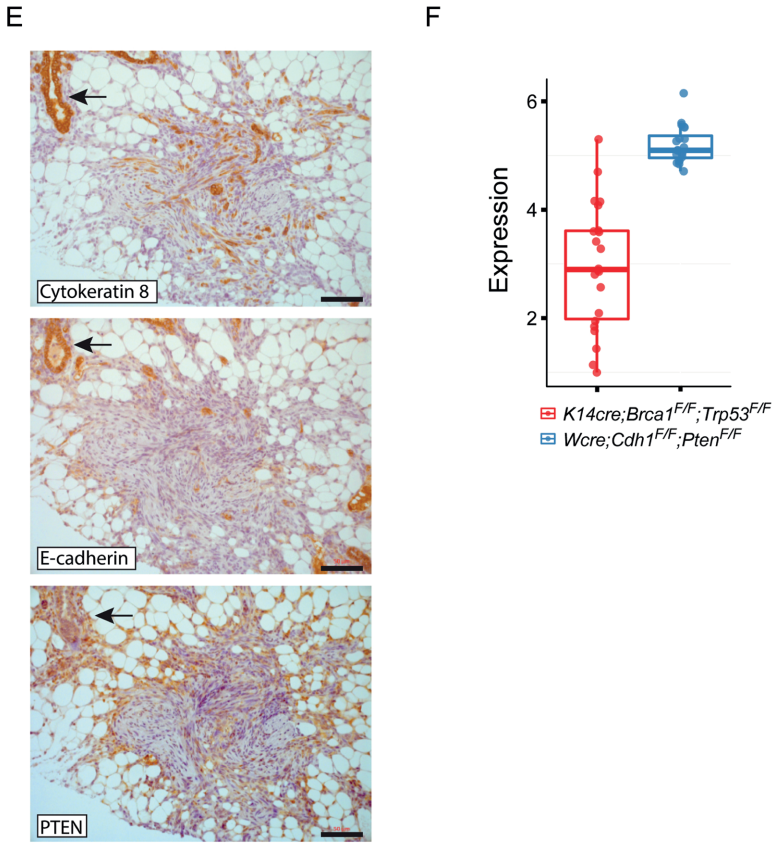

Supplemental Figure S3. Somatic inactivation of E-cadherin and PTEN induces mammary tumors that closely resemble human CLC

(A) Mammary tumor specific survival plot of *Wcre;Pten*$^{F/+}$ (n=26), *Wcre;Cdh1*$^{F/F}$ (n=39), *Pten*$^{F/+}$ (n=23), *Wcre;Pten*$^{F/F}$ (n=21) and *Wcre;Cdh1*$^{F/F}$*;Pten*$^{F/F}$ (n=60) mice, revealing decreased survival of *Wcre;Cdh1*$^{F/F}$*;Pten*$^{F/F}$ compared to *Wcre;Pten*$^{F/F}$ mice (p<0001). Latencies are depicted in days of age. (B) Representative images of IHC staining for p-AKT, p-4ebp1 and p-S6 in tumor cells of mCLC in *Wcre;Cdh1*$^{F/F}$*;Pten*$^{F/F}$ mice, confirming activation of PI3K signaling. Bar=50µm. (C) Representative images of IHC staining for ERα of mammary gland sections with mCLC in *Wcre;Cdh1*$^{F/F}$*;Pten*$^{F/F}$ mice to exemplify the differences in cell morphology between neoplastic cells (encircled by a dashed line) and surrounding stromal cells that were used to score the ER+ tumor cells. Bar=50µm. (D) Representative examples of mammary tumors classified as solid ILC, solid carcinoma, squamous metaplastic carcinoma and EMT as determined by H&E and IHC staining of CK8, CK1, Vimentin, E-cadherin and PTEN. Arrows highlight E-cadherin or PTEN proficient cells. Bar=25µm. (E) Representative IHC staining for CK8, Ecadherin and PTEN in mammary tumors from 12-week-old *Wcre;Cdh1*$^{F/F}$*;Pten*$^{F/+}$ mice. The arrow highlights CK8-marked luminal cells expressing E-cadherin and PTEN in the mammary duct, in contrast to CK8-marked tumor cells in the adjacent lesion, which lost E-cadherin and PTEN protein expression. Bar=100µm. (F) *Esr1* mRNA expression levels extracted from RNA sequencing data of mammary tumors from *K14cre;Brca1*$^{F/F}$*;Trp53*$^{F/F}$ (n=22) and *Wcre;Cdh1*$^{F/F}$*;Pten*$^{F/F}$ (n=20) mice and compared to FACS-sorted Epcam-positive tumor cells from *Wcre;Cdh1*$^{F/F}$*;Pten*$^{F/F}$ mammary tumors (n=18).

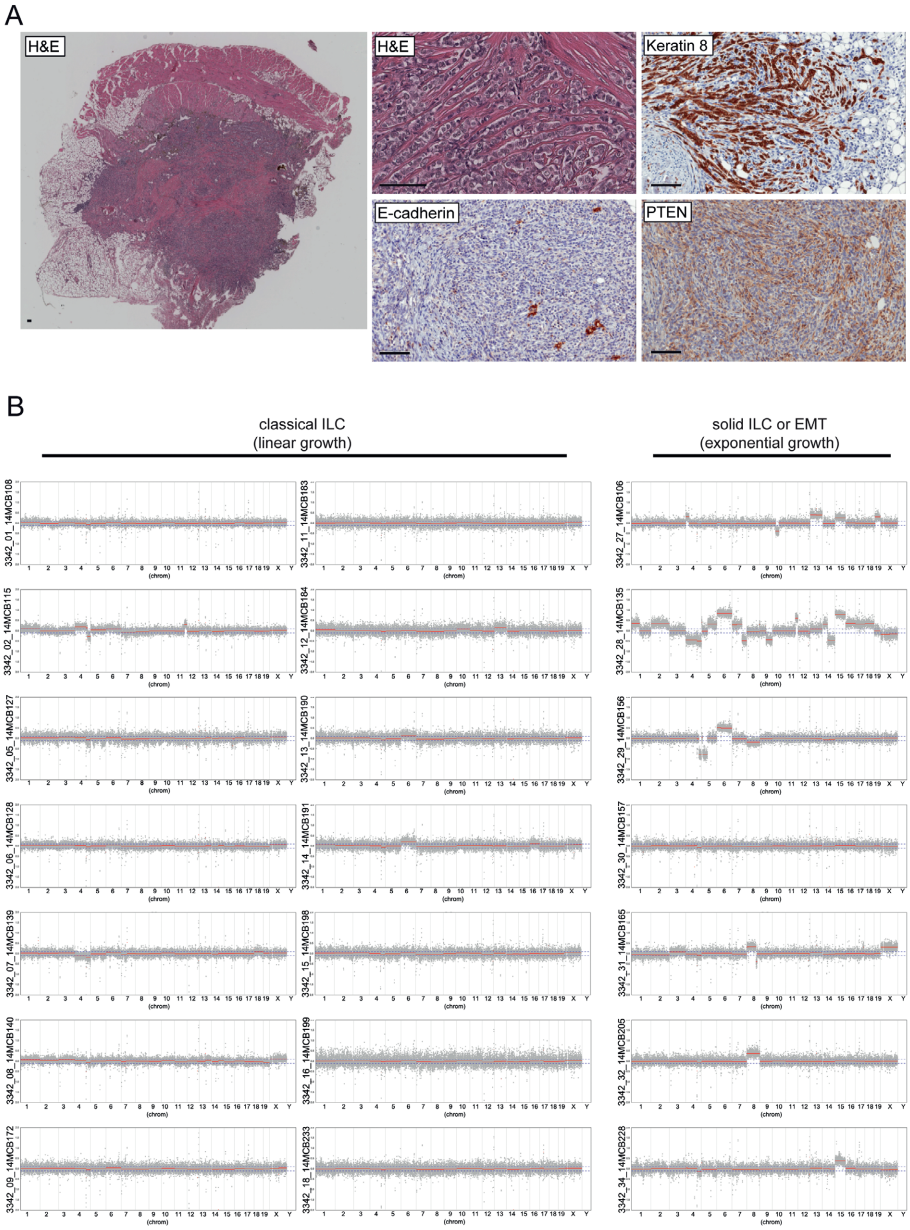

Supplemental Figure S4. Characterization of mammary tumors from mice transplanted with precancerous *Wcre;Cdh1$^{F/F}$;Pten$^{F/F}$* mammary gland fragments

(A) Representative images of IHC staining of CK8, E-cadherin and PTEN in tumors from mice transplanted with precancerous *Wcre;Cdh1$^{F/F}$;Pten$^{F/F}$* mammary gland fragments. Bar=100µm. (B) DNA copy-number profiles of linear-growing mCLCs (n=14) and exponential-growing solid ILCs and EMT tumors (n=7) from mice transplanted with precancerous *Wcre;Cdh1$^{F/F}$;Pten$^{F/F}$* mammary gland fragments.

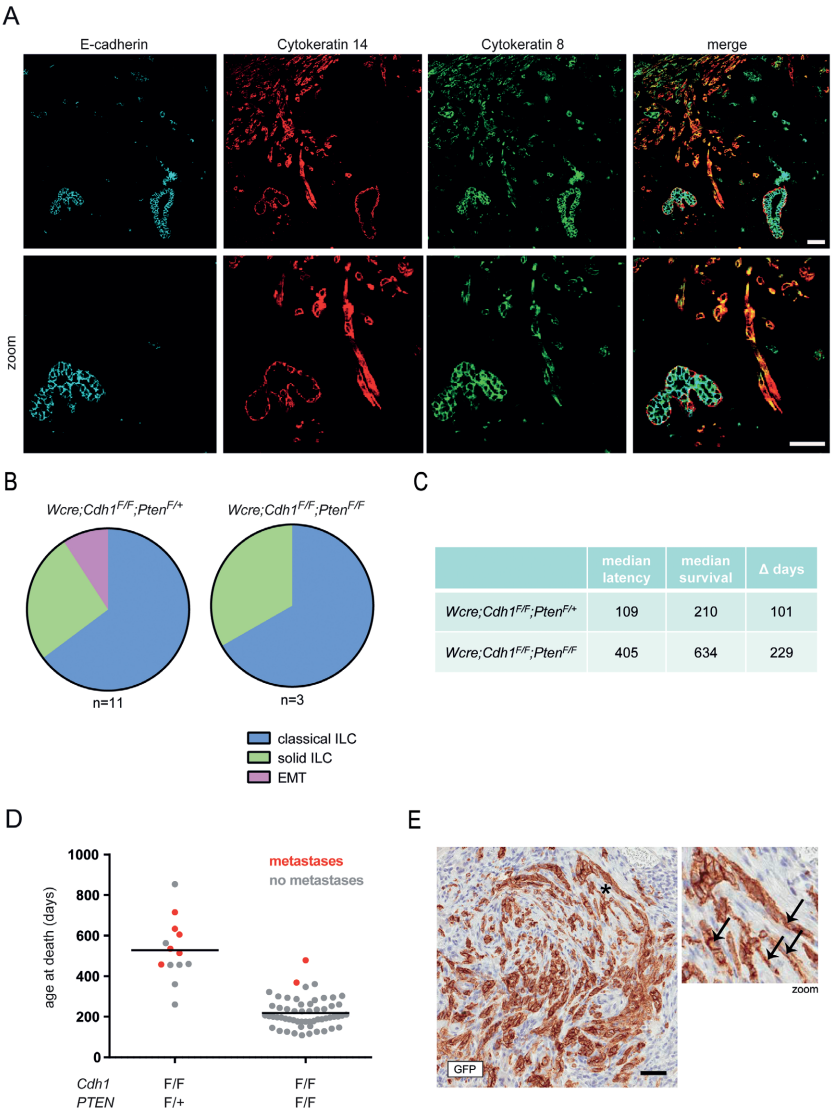

	median latency	median survival	Δ days
Wcre;Cdh1$^{F/F}$;Pten$^{F/+}$	109	210	101
Wcre;Cdh1$^{F/F}$;Pten$^{F/F}$	405	634	229

Supplemental Figure S5. Metastatic behavior of *Wcre;Cdh1$^{F/F}$;Pten$^{F/F}$* mammary tumors

(A) IF analyses of mammary tumors by immunostaining of CK8, CK14 and E-cadherin revealing dual positive CK8/CK14 tumor cells at the invasive front of mammary tumors obtained from 12-week-old *Wcre;Cdh1$^{F/F}$;Pten$^{F/F}$* mice. Bar=50µm (B) Pie charts reflecting the primary tumor phenotype of metastasis-harboring *Wcre;Cdh1$^{F/F}$;Pten$^{F/+}$* (n=11) and *Wcre;Cdh1$^{F/F}$;Pten$^{F/F}$* (n=3) mice. (C) Analyses of median tumor latency and median survival of *Wcre;Cdh1$^{F/F}$;Pten$^{F/+}$* and *Wcre;Cdh1$^{F/F}$;Pten$^{F/F}$* mice to compare average days of time between tumor detection and sacrifice of the mice. (D) Age at death and metastatic status plotted for *Wcre;Cdh1$^{F/F}$;Pten$^{F/+}$* and *Wcre;Cdh1$^{F/F}$;Pten$^{F/F}$* mice to examine the correlation between life span and metastatic incidence. (E) IHC staining for GFP in tumor cells of mCLCs from *Wcre;Cdh1$^{F/F}$;Pten$^{F/F}$;mTmG* mice. Bar = 25µm.

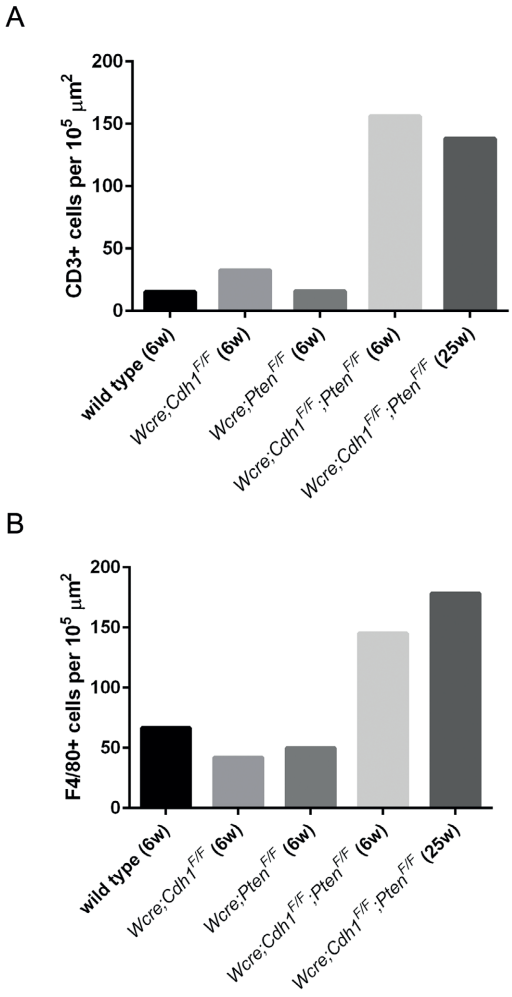

Supplemental Figure S6. Quantification of stromal components in mouse CLC

(A) Quantification of IHC staining of CD3-marked immune cells in mammary gland sections of wildtype, *Wcre;Cdh1*$^{F/F}$, *Wcre;Pten*$^{F/F}$ and *Wcre;Cdh1*$^{F/F}$*;Pten*$^{F/F}$ mice, displayed as number of cells per 105 µm2 analyzed mammary gland area. (B) Quantification of IHC staining of F4/80-marked macrophages in mammary gland sections of wildtype, *Wcre;Cdh1*$^{F/F}$, *Wcre;Pten*$^{F/F}$ and *Wcre;Cdh1*$^{F/F}$*;Pten*$^{F/F}$ mice displayed as number of cells per 105 µm2 analyzed mammary gland area.

Supplemental Table 1. Identified oncogenic mutations by exome sequencing, related to figure 4.

#	Tumor phenotype	Gene symbol	Cds position	Nucleotide substitution	Protein position	Amino acids	Consequence	Allele freq
1	EMT	Ccnd3	850	Ccc/Tcc	284	P/S	missense	0.333
2	Solid ILC	Kras	38	gGc/gAc	13	G/D	missense	0.588
3	Solid ILC	Asxl1	1979	ggA/gg	639	G/X	frameshift	0.436
4	EMT	Myh9 Ptpn11	232-244 188	CCAAGTTCTCCAag/ag tAt/tGt	78-82 63	PFKXK/X Y/C	frameshift missense	0.269 0.448
5	EMT	Trp53	808	Cgt/Tgt	270	R/C	missense	0.496
6	EMT	Pwwp2a Ptpn11	2111 1532	cGc/cAc aCa/aAa	704 511	R/H T/K	missense missense	0.297 0.302
7	EMT	Ptpn11	1393	Gct/Act	465	A/T	missense	0.222

Supplemental Table 2. Antibodies used in this study.

Antibody	Manufacturer	Application	Species	Antigen retrieval	Dilution
Akt	Cell Signaling #9272	WB	mouse	NA	1:1000
Cleaved Caspase 3	Cell Signaling #9661	IF	mouse	TRIS/EDTA pH9.0	1:100
CD3	Thermo Scientific RM-9107	IHC	mouse	TRIS/EDTA pH9.0	1:600
CD3	Thermo Scientific RM-9107	IHC	human	Cell Conditioning 1	1:100
CD68	DAKO M0814	IHC	human	Cell Conditioning 1	1:2000
Cytokeratin 1	Covance PRB-165P	IHC	mouse	Citrate pH6.0	1:200
Cytokeratin 8	DSHB Univ of Iowa TROMA-1	IHC	mouse	Citrate pH6.0	1:800
Cytokeratin 8	DSHB Univ of Iowa TROMA-1	IF	mouse	TRIS/EDTA pH9.0	1:200
Cytokeratin 14	Covance PRB-155P	IF	mouse	TRIS/EDTA pH9.0	1:200
E-cadherin	Cell Signaling #3195	IHC	mouse	TRIS/EDTA pH9.0	1:200
E-cadherin	BD Biosciences #610181	IF	mouse	TRIS/EDTA pH9.0	1:100
E-cadherin	BD Biosciences #610181	WB	mouse	NA	1:1000
ERα	Santa Cruz sc-542	IHC	mouse	TRIS/EDTA pH9.0	1:2000
F4/80	Serotec MCA497	IHC	mouse	Proteinase K	1:400
HSP90	Santa Cruz sc-9747	WB	mouse	NA	1:2000
Ki-67	Cell Signaling #9449	IF	mouse	Citrate pH6.0	1:100
PDGFRβ	Cell Signaling #3169	IHC	mouse	TRIS/EDTA pH9.0	1:50
PDGFRβ	Abcam ab32570	IHC	human	Cell Conditioning 1	1:100
phospho-Akt	Cell Signaling #4060	IHC	mouse	Citrate pH6.0	1:8000
phospho-Akt	Cell Signaling #4060	WB	mouse	NA	1:2000
phospho-S6	Cell Signaling #2211	IHC	mouse	Citrate pH6.0	1:400
phospho-S6	Cell Signaling #2211	WB	mouse	NA	1:1000
PTEN	Cell Signaling #9559	IHC	mouse	Citrate pH6.0	1:100
PTEN	Cell Signaling #9188	IF	mouse	TRIS/EDTA pH9.0	1:100
PTEN	Cell Signaling #9188	WB	mouse	NA	1:1000
S6	Cell Signaling #2217	WB	mouse	NA	1:1000
Vimentin	Cell Signaling #5741	IHC	mouse	TRIS/EDTA pH9.0	1:200

SUPPLEMENTAL EXPERIMENTAL PROCEDURES

Isolation of primary mammary epithelium and organoid generation

In brief, mammary glands were harvested from 8- to 12-week-old FVB mice, minced with a pair of scissors, and shaken for 20 min at 37°C in collagenase solution: DMEM (10565–018; Gibco) with 2 mg/ml Collagenase type IV (17104-019; Gibco), 2 mg/ml trypsin (27250–018; Gibco), 5% FBS (F0926; Sigma-Aldrich), 5 µg/ml insulin (I9278; Sigma-Aldrich), and 50 µg/ml gentamicin (15750; Gibco). Suspensions were centrifuged at 1500 rpm to remove a floating layer of adipocytes, and pellets were treated with 2 U/µl DNase (D4263; Sigma-Aldrich) to detach organoids from stromal cells. Enzymes and single cells were removed by four spins of 1 min at 1500rpm by which pellets were obtained that mainly contained small mammary epithelial fragments (organoids). Organoids were embedded in Matrigel (354230; BD) and plated as 100-µl suspensions in Millicell Ezslide 8-well Glass wells (PEZGS0816; Millipore). Gels were allowed to polymerize for 30 min at 37°C before supplementing organoid medium: DMEM with 1% insulin-transferrin-selenium (51500–056; Gibco) and 1% penicillin-streptomycin (P4333; Sigma-Aldrich). Images of organoids were obtained by using the Axio Observer Z1 ZEISS microscope. To obtain organoid growth, organoid size was measured weekly using the ZEISS ZEN Software. Organoid whole-mount imaging was performed by removing culture medium to wash and fix the organoids in 3.7% Paraformaldehyde at RT for 30'. Organoids were permeabilized with 1% Triton X-100, 10% glycerol in PBS for 30 min at RT. Organoids were incubated with primary antibody against; Rabbit Cleaved Caspase-3 (1:100, Cell Signaling #9661) and mouse ki67 (1:100, Cell Signaling #9449) in PBS containing 0.1% triton and 10% glycerol o/n at 4°C. Organoids were subsequently washed 3 times with PBS and stained with secondary antibodies anti-Rabbit-AlexaFluor 568 (1:500, Invitrogen #A11011) and anti-mouse-AlexaFluor 488 (1:500, Molecular Probes #A21141) and Hoechst o/n at 4°C. Organoids were subsequently washed and mounted using Vectashield (Vector Laboratories H-1000). Images were acquired using a Leica TCS SP5 Confocal and images were analyzed using LAS AF Version 2.6.3 software.

Adenoviral delivery of Cre recombinase

Before embedding in Matrigel, Adcre was added to isolated mammary organoids to drive Cre-recominase activity during subsequent organoid development in matrigel (1×108 Transducing Units (TU); Gene Transfer Vector Core, University of Iowa). Seven days later, DNA was isolated using direct PCR lysis buffer (301-C; Viagen) to analyze Cre-driven recombination efficiency, and protein was isolated using NP40 lysis buffer

(20 mM Tris pH 7.4, 100 mM NaCl, 1% NP40, 10% glycerol, 10 mM EDTA complemented with protease inhibitors (Roche) to analyze inactivation of E-cadherin and/or PTEN.

Immunoblotting

Tissue was homogenized using a microhomogenizer and protein lysates were prepared using a RIPA lysis buffer (20mM Tris pH 8.0, 300mM NaCl, 10mM EDTA, 20% glycerol, 2% NP40) supplemented with protease and phosphatase inhibitors (Roche) and quantified using the BCA Protein Assay Kit (Pierce). Equal amounts of protein were separated by 4-12% SDS-PAGE (Invitrogen), transferred onto a nitrocellulose membrane (Biorad), blocked with 5% BSA in PBS-Tween (0.05%), and probed for primary antibodies as listed in Table S1 and secondary antibodies HRP goat-anti-rabbit (DAKO). Protein was visualized using ECL (Pierce ECL-Western blotting 32106).

Histopathology

Mouse tissues were formalin-fixed in 10% neutral buffered formalin for 48 hours, embedded in paraffin, sectioned and stained with hematoxylin and eosin (H&E) or Masson's trichrome. IHC was performed as previously described (Henneman et al., 2015). Primary antibody details and antigen retrieval methods are described in Supplemental information Table S1. Secondary antibodies that were used are HRP anti-rabbit Envision (DAKO K4011), Biotin anti-rabbit (DAKO E0432), and Biotin anti-rat (Santa Cruz sc-2041). All slides were digitally processed using the Aperio ScanScope (Aperio, Vista, CA, USA) and captured using ImageScope software version 12.0.0 (Aperio).

Immunofluorescence

Formalin-fixed and paraffin-embedded sections were processed as described (Pasic *et al.,* 2011) and incubated overnight at 4°C with primary antibodies. Antibody details and antigen retrieval methods are described in Supplemental Table S1. Secondary antibodies anti-Rat-AlexaFluor 647 (1:1000, Invitrogen #A21247), anti-Rabbit-AlexaFluor 568 (1:1000, Invitrogen #A11011) and anti-mouse-AlexaFluor 488 (1:1000, Molecular Probes #A21141) were incubated overnight at 4°C. Sections were subsequently stained with Hoechst (1:1000, Thermo Scientific #62249) for 5 min and mounted using Vectashield (Vector Laboratories H-1000). Images were acquired using a Leica TCS SP5 Confocal and analyzed using LAS AF Version 2.6.3 software.

Whole-mount staining

Inguinal mammary glands were dissected, fixed for 4 hours in methacarn (60% methanol, 30% chloroform, 10% acetic acid), and subsequently stained overnight in 0.2% carmine alum. After dehydration in 70%, 90% and 100% ethanol series, the glands were cleared in xylene and photographed using an Olympus SZX12 microscope.

RNA sequencing

Total tumor tissues were homogenized in TRIzol reagent (15596-018, Ambion life technologies) using a polytron (DI 18 Disperser, IKA) according to the manufactures protocol. Briefly, 0.2x volumes of chloroform (Chloroform stab./Amylene, Biosolve) was added to the homogenate and the tube(s) were shaken vigorously. The tube(s) were incubated for 2-3 minutes at room temperature and centrifuged (Hettich, rotanta 46 RS) for 1 hour (4120 RCF, 4 °C). Approximately 70% of the upper aqueous phase was transferred to a clean 15 mL tube and 0.5x volume of isopropanol (33539, Sigma-Aldrich,) was added. The tube(s) were incubated overnight at -20 °C and centrifuged for 30 minutes (4120 RCF, 4 °C). The supernatant was removed and the pellet was washed twice with 80% ethanol (32221-2.5L, Sigma-Aldrich). The total RNA pellet was air-dried and dissolved in an appropriate volume of nuclease free water (AM9937, Ambion life technologies) and quantified using Nanodrop UV-VIS Spectrophotometer (Thermo Fisher Scientific Inc.). Total RNA was purified using the MinElute Cleanup Kit (74204, Qiagen) according to the manufactures instructions. Quality and quantity of the total RNA was assessed by the 2100 Bioanalyzer using a Nano chip (Agilent, Santa Clara, CA). Total RNA samples having RIN>8 were subjected to library generation.

Illumina TruSeq mRNA libraries were generated using the TruSeq RNA Library Preparation Kit v2 sample preparation kit (Illumina Inc., San Diego, Cat.No RS-122-2001/2) according to the manufacturer's instruction (Part #15026495 Rev. B) Briefly, polyadenylated RNA from intact total RNA was purified using oligo-dT beads. Following purification the RNA was fragmented, random primed and reverse transcribed using SuperScript II Reverse Transcriptase (Invitrogen, part # 18064-014). Second strand synthesis was accomplished by using Polymerase I and RNaseH. The generated cDNA fragments were 3' end adenylated and ligated to Illumina Paired-end sequencing adapters and subsequently amplified by 15 cycles of PCR. The libraries were analyzed on a 2100 Bioanalyzer using a 7500 chip (Agilent, Santa Clara, CA), diluted and pooled equimolar into a 10nM sequencing pool containing 8-10 samples each. The libraries were sequenced with 50 base single reads on a HiSeq2000 using V3 chemistry (Illumina Inc., San Diego). The obtained data will available for future analysis at www.xxx.org.

Generating PAM50 signature of mCLC

In order to investigate molecular similarities between mCLC from *Wcre;Cdh1*$^{F/F}$*;Pten*$^{F/F}$ mice and human breast cancer samples, the TCGA BRCA dataset was integrated with RNAseq data of mouse mammary tumor samples from *Wcre;Cdh1*$^{F/F}$*;Pten*$^{F/F}$ and *K14cre;Brca1*$^{F/F}$*;Trp53*$^{F/F}$ mice. Gene expression profiles for each sample were collected from RNAseq data normalized by TMM (Robinson and Oshlack, 2010). Batch effects were corrected using ComBat (Johnson et al., 2007). Unsupervised hierarchical clustering was performed using genes from the PAM50 signature (Parker et al., 2009).

Whole-exome sequencing

Due to high stromal contamination in mCLC, the tumor cell population was enriched through FACS-sorting based on expression of epithelial marker EpCAM. Tumor tissues of *Wcre;Cdh1*$^{F/F}$*;Pten*$^{F/F}$ mice were processed as described above. Single cells were stained with directly conjugated EpCAM-FITC (eBioscience 11-5791) for 30 min at 4 °C in the dark in PBS/1% BSA. DAPI (1:20) was added to exclude dead cells. EpCAM-positive cells were collected using a BD FACSAria IIu flow cytometer. Genomic DNA was isolated from this cell population using QIAamp DNA micro kit (Qiagen) according to manufacturer's instructions. For exponentially growing non-CLC tumor tissue, genomic DNA was isolated using proteinase K lysis and phenol-chloroform organic extraction. For whole-exome sequencing, up to 2 ug of genomic DNA samples was sheared to a length between the 200-300 bp using the covaris S2 system. The sheared DNA samples were cleaned using 1.8x of the Agencourt Ampure XP beads (part.no A63881). The DNA library preparation was performed with the Kapa HTP DNA library preparation kit (KK8234), according to protocol. Input library prep sample of FACS-sorted CLC tumor samples was 5-150 ng dsDNA; Input library prep sample of non-CLCs was 1000 ng dsDNA. The enrichment assay was performed using the SureSelect XT2 Mouse All Exon kit (part no. 5190-4681). One adjustment to the hybridization protocol was made, we used a 1:1 diluted Mouse All Exon capture library. The obtained data will available for future analysis at www.xxx.org.

Extraction of mutations from whole-exome sequencing data

Sequence reads from the exome capture were mapped to the mouse reference genome (mm10), using BWA (Li and Durbin, 2009). The mapped sequence reads were further processed according to GATK best practices using Picard (version 1.128) and GATK (version 3.4) (Van der Auwera et al., 2013) to perform duplicate marking, indel realignment and base quality score recalibration. SNPs and indels were called from

these processed alignments using HaplotypeCaller (version 3.4.0). Variants were filtered to remove calls from sequencing artefacts using GATKs recommended practice for hard-filtering of variant calls. To remove variants that are part of the mouse background, we filtered variants that were known FVB variants (Wong et al., 2012) and variants that occurred with a variant allele frequency greater than 0.1 in at least one sample in a panel of four normal (spleen) samples. The remaining variants were then annotated using VEP and filtered to select only deleterious variants (missense variants, frame shift variants, stop gained/lost variants and UTR variants). To prioritize cancer-related variants, these variants were annotated for their presence in the Cancer Gene Census (Futreal et al., 2004).

CNV analysis

We used the CopywriteR tool (Kuilman et al., 2015) to obtain copy number profiles from the exome alignments, which effectively extracts off-target reads from the exome capture and uses these to estimate copy number profiles. The log2 copy number estimates from CopywriteR were smoothed and segmented using the circular binary segmentation (CBS) algorithm as implemented in the DNACopy R package (Venkatraman and Olshen, 2007). In this segmentation, segments that were smaller than 5 probes or that deviated less than 3 standard deviations were pruned to reduce the number of spurious segments. For each sample, we then centered the (log2) copy number estimates of these segments by subtracting the segment copy number value in each sample. Using these centered values, we then determined the number of chromosomal aberrations in each sample as the number of segments with copy number values above 0.1 or below -0.1. To remove systematic artefacts from the copy number calling and/or segmentation, we did not count any segments that were present in more than 15 samples. Similarly, to further reduce the noise in the counts, we removed segments that spanned less than 10 probes, as these were considered more likely to represent noise than actual focal amplifications/deletions.

SUPPLEMENTAL REFERENCES

Johnson, W.E., Li, C., Rabinovic, A., 2007. Adjusting batch effects in microarray expression data using empirical Bayes methods. Biostatistics 8, 118–127.

Futreal, P.A., Coin, L., Marshall, M., Down, T., Hubbard, T., Wooster, R., Rahman, N., Stratton, M.R., 2004. A census of human cancer genes. Nat. Rev. Cancer 4, 177–183.

Kuilman, T., Velds, A., Kemper, K., Ranzani, M., Bombardelli, L., Hoogstraat, M., Nevedomskaya, E., Xu, G., de Ruiter, J., Lolkema, M.P., Ylstra, B., Jonkers, J., Rottenberg, S., Wessels, L.F., Adams, D.J., Peeper, D.S., Krijgsman, O., 2015. CopywriteR: DNA copy number detection from off-target sequence data. Genome Biol. 16, 49.

Li, H., Durbin, R., 2009. Fast and accurate short read alignment with Burrows-Wheeler transform. Bioinformatics 25, 1754–1760.

Parker, J.S., Mullins, M., Cheang, M.C.U., Leung, S., Voduc, D., Vickery, T., Davies, S., Fauron, C., He, X., Hu, Z., Quackenbush, J.F., Stijleman, I.J., Palazzo, J., Marron, J.S., Nobel, A.B., Mardis, E., Nielsen, T.O., Ellis, M.J., Perou, C.M., Bernard, P.S., 2009. Supervised risk predictor of breast cancer based on intrinsic subtypes. J. Clin. Oncol. 27, 1160–1167.

Van der Auwera, G.A., Carneiro, M.O., Hartl, C., Poplin, R., Del Angel, G., Levy-Moonshine, A., Jordan, T., Shakir, K., Roazen, D., Thibault, J., Banks, E., Garimella, K.V., Altshuler, D., Gabriel, S., DePristo, M.A., 2013. From FastQ data to high confidence variant calls: the Genome Analysis Toolkit best practices pipeline. Curr. Protoc. Bioinformatics 11, 1–33.

Venkatraman, E.S., Olshen, A.B., 2007. A faster circular binary segmentation algorithm for the analysis of array CGH data. Bioinformatics 23, 657–663.